

# Numerical Heat Transfer, Part A: Applications

## An International Journal of Computation and Methodology

ISSN: (Print) (Online) Journal homepage: <https://www.tandfonline.com/loi/unht20>

---

# Role of Lorentz force and nanoparticles morphology on the dynamics of ternary hybrid nanofluid flow subject to porous disks and gyrotactic microorganisms

Qadeer Raza, Xiaodong Wang, Fahad Ullah Khan & Ali J. Chamkha

To cite this article: Qadeer Raza, Xiaodong Wang, Fahad Ullah Khan & Ali J. Chamkha (11 Dec 2023): Role of Lorentz force and nanoparticles morphology on the dynamics of ternary hybrid nanofluid flow subject to porous disks and gyrotactic microorganisms, Numerical Heat Transfer, Part A: Applications, DOI: [10.1080/10407782.2023.2290084](https://doi.org/10.1080/10407782.2023.2290084)

To link to this article: <https://doi.org/10.1080/10407782.2023.2290084>



Published online: 11 Dec 2023.



Submit your article to this journal [↗](#)





View related articles [↗](#)



View Crossmark data [↗](#)



# Role of Lorentz force and nanoparticles morphology on the dynamics of ternary hybrid nanofluid flow subject to porous disks and gyrotactic microorganisms

Qadeer Raza<sup>a</sup> , Xiaodong Wang<sup>a</sup>, Fahad Ullah Khan<sup>b</sup>, and Ali J. Chamkha<sup>c</sup> 

<sup>a</sup>School of Mathematics and Statistics, Xi'an Key Laboratory of Scientific Computation and Applied Statistics, Northwestern Polytechnical University, Xi'an, China; <sup>b</sup>Department of Management Science and Engineering, Northwestern Polytechnical University, Xi'an, China; <sup>c</sup>Faculty of Engineering, Kuwait College of Science and Technology, Kuwait

## ABSTRACT

This article explains the significance of Lorentz force and nanoparticle morphology on the dynamics of ternary hybrid nanofluid through porous disks. The gyrotactic microorganisms are investigated to avoid possible sedimentation of solid particles and maintain fluid stability. A 3-dimensional flow problem in the presence of two different types of tri-hybrids nanofluid nanomaterials (Metallic and Nonmetallic Oxides) is used here. By eliminating the pressure term, the governing partial differential equations are transformed into a high-order nonlinear system of differential equations. This system is subsequently utilized to construct the boundary layer model, and these equations are solved numerically using a shooting technique based on the Runge–Kutta method, with the assistance of MATLAB software. The comparison and validation results are in good agreement through a numerical approach. Different-shaped nanoparticles have a significant influence on motile microorganisms. Shear stress near porous surfaces was significantly reduced due to an increase in nanoparticle size. The addition of all types of nanoparticles improved the thermal performance. Many desirable results for engineering purposes are observed under suitable conditions of simultaneous effect of magnetohydrodynamics (MHD) with microorganisms.

## ARTICLE HISTORY

Received 31 May 2023  
Revised 5 November 2023  
Accepted 24 November 2023

## KEYWORDS

3-dimensional heat and mass transfer; hybrid and ternary hybrid nanofluids; shape and size factor

## 1. Introduction

Today, the utilization of nanoparticles in a base fluid to enhance the thermal performance of fluid has gotten a lot of consideration. The applications of nanofluids are engineering problems, heating-ventilation-air conditioning (HVAC), atomic reactors, heat transmission, heat pipes, solar energy, and equipment airflow. These innovative fluids combine metallic, nonmetallic, and polymeric nano-sized powders into a base fluid, yielding improved properties. The creation of ternary-hybrid nanoparticles involves incorporating distinct nanoparticles into a single ternary hybrid (trihybrid) nanoparticle, utilizing nanoparticles selected based on their rheological and thermo-physical characteristics. This approach offers numerous benefits, such as heightened thermal conductivity, increased stability within base liquids, larger surface areas, improved crystallinity, and enhanced zeta potentials. For instance, Shamshuddin et al. [1] explored energy transfer in a ternary hybrid nanofluid featuring copper (Cu), iron oxide ( $\text{Fe}_3\text{O}_4$ ), and silicon dioxide ( $\text{SiO}_2$ )

## Nomenclature

$B_0$	Uniform magnetic field [T]	$\rho C_p$	Volumetric heat capacity [J/(m <sup>3</sup> K)]
$g[\eta]$	Dimensionless tangential velocity profile	T	Temperature [K]
$C_f$	Total skin friction coefficient	$Nn_z$	Motile microorganisms
$C_p$	Specific heat at constant pressure	Pe	Peclet number
$s$	Time depended on the coefficient	$(\rho c_p)_{trihnf}$	Specific heat capacity for tri hybrid nanofluid
M	Magnetic parameter	$\rho_{s1}$	Density for first solid nanoparticle
Pr	Prandtl number	$\rho_{s2}$	Density for second solid nanoparticle
r z	Cylindrical coordinates system	$k_{nf}$	Thermal conductivity for nanofluid
Re	Reynolds number	$k_{s1}$	Thermal conductivity for first solid fraction
$\gamma$	The ratio of density in motile microorganisms	$k_{s3}$	Thermal conductivity for third solid fraction
$A_1$	Dimensional less parameter	$\mu_{trihnf}$	Viscosity of tri hybrid nanofluid
u, v, w	Velocity component along (r,0,z) axis	$\nu_{trihnf}$	Kinematics viscosity for tri hybrid nanofluid
Nu	Nusselt number	<b>Greek Symbols</b>	
$\rho_{trihnf}$	Density for tri hybrid nanofluid	$\alpha$	Thermal diffusivity [m <sup>2</sup> /s]
$\rho_{s3}$	Density for third solid nanoparticle	$\varphi$	Equivalent nanoparticles volume fraction
$k_{trihnf}$	Thermal conductivity for tri hybrid nanofluid	$\varphi_2$	Equivalent 2nd nanoparticles volume fraction
$k_{s2}$	Thermal conductivity for second solid fraction	$\eta$	Independent similarity variable
p	Pressure	$\varphi_1$	Equivalent first nanoparticles volume fraction
$k_{bf}$	Thermal conductivity for base fluid	$\varphi_3$	Equivalent 3rd nanoparticles volume fraction
$f'[\eta]$	Dimensionless radial velocity profile		
Sc	Schmidt number		
$\theta[\eta]$	Dimensionless temperature profile		
$\sigma$	Electrical conductivity [(m <sup>3</sup> A <sup>2</sup> )/kg]		
$\nu$	Kinematic viscosity [m <sup>2</sup> /s]		
$\mu$	Dynamic viscosity [Pa·s]		
$\rho$	Density [kg/m <sup>3</sup> ]		

nanoparticles suspended in a polymer-based base fluid. They observed the fluid's movement along a spinning disk surface. In another study, Alharbi et al. [2] investigated the motion of an electrically conducting incompressible ternary hybrid nanofluid around an elongated cylinder under the influence of magnetic induction. This research considered heat conduction within a border layer containing metallic nanoparticles (NPs). Moreover, Alshahrani et al. [3] analyzed the movement of ternary hybrid nanofluids across a rotating disk with thermal radiation effects, steady magnetic fields, and slip boundary conditions. In the present study, an impermeable rotating disk interacts with an immiscible ternary hybrid nanofluid (NF) comprising aluminum oxide (Al<sub>2</sub>O<sub>3</sub>), copper oxide (CuO), and titanium dioxide (TiO<sub>2</sub>) nanoparticles. Usman et al. [4] examine the effect of a time-varying magnetic field on the unsteady slip flow of a trihybrid nanofluid across an inclined spinning disk, as well as the related heat transfer process. Ali et al. [5] examined second law analysis in the context of stagnation point flow on a flexible spinning disk utilizing a ternary hybrid nanofluid. Gupta et al. [6] studied the three-dimensional magneto stagnation-point movement of a trihybrid nanofluid affected by a radially stretched gyrating disk with various slip characteristics. The research conducted by Puneeth et al. [7] delved into the heat and mass transfer characteristics of trihybrid nanofluids generated by suspending three distinct nanoparticles. Additionally, Sarangi et al. [8] explored the improved heat transfer and flow efficiency achieved using ternary composite nanomaterials compared to mono and hybrid nanofluids under second-order slip conditions. According to Alanazi et al. [9], the analysis involves a study of 3D flow across rotating porous disks along with a ring-shaped sector, employing fully developed hybrid nanofluids. Tassaddiq et al. [10] conducted research on an infinitely long impermeable spinning disk.

Magnetic field effects were incorporated to delve into the intricacies of nanofluid flow. In a different context, Zhang et al. [11] focused on a three-dimensional numerical formulation of an unbalanced Ag-MgO/water hybrid nanofluid flow generated by an oscillating, wavy spinning disk. Investigating an unstable flow within a spinning disk featuring a hybrid nanofluid with vacuum and retardation characteristics was the objective of Waini et al. [12]. Agrawal et al. [13] evaluated the efficiency of thermal conduction and the flow properties of hybrid nanofluids between two parallel disks. Alahmadi and Alkinidri [14] conducted a study on the significance of nanoparticles in thermal transmission, considering the Carreau-Yasuda fluid phenomena and bioconvective phenomena. Iqbal et al. [15] analyzed the thermal transmission of nanomaterials with Eyring-Powell fluid properties, accounting for variable thermal characteristics and the peristaltic motion of gyrotactic microorganisms. Akbar et al. [16] conducted a comprehensive study on the magnetic field flow of a stretching and shrinking sheet, considering slip effects. Khan et al. [17] presented a cohesive study on the irreversibility of Ellis hybrid fluid flow with Copper and Aluminum nanoparticles, incorporating catalyzed reactions and multiple slip effects. Ahmad et al. [18] researched the MHD Casson hybrid nanofluid flow while considering interference in thermal conductivity over a stretching cylinder. Nadeem et al. [19] analyzed nanofluid stream characteristics, including mixed convective hybrid nanoparticles inclusion, and focused on Thomson and Troian slip conditions. Ahmad et al. [20] examined the impact of bio-convection hybridization on micropolar nanofluid flow under stratification conditions over a vertically exponentially stretched surface. The study by Bejawada and Nandeppanavar [21] investigated MHD temperature transfer considering radiation effects in micropolar fluid flow over a vertically porous moving plate. Khan et al. [22] explored the effects of homogeneous-heterogeneous chemical reactivity on second-grade nanofluids and gyrotactic microorganisms in a rotating sphere, while also considering thermal radiation effects.

Bioconvection is a natural phenomenon where microorganisms move collectively or individually. This motion can be directed, and it has applications across biotechnology and petrochemical fields. The presence of microorganisms affects fluid dynamics by enhancing the fundamental frequency and creating frequency gradients through floating, giving bioconvection an advantage. Microorganisms' behavior is influenced by forces like gyrotactic, oxytactic, and gravitactic effects, which can vary based on the type of microbe. The properties of nanoparticles also interact with microorganisms, finding applications in Immunology Microsystems involving enzyme biosensors, protein engineering, fabricated biology, tissue engineering, and drug distribution systems. Several researchers have contributed to this field, some of whose work is noteworthy. For example, Bilal et al. [23] conducted a numerical simulation using a wavy disk to study ferric oxide water-based hybrid nanofluid flows, incorporating carbon nanotubes (CNTs) and motile microbes. Waqas et al. [24] presented the bioconvection behavior of a Casson nanofluid around a circular disk with gyrotactic motile microorganisms, various slips, and heat radiation. Naveed et al. [25] explored the boundary layer flow of a hybrid nanofluid containing gyrotactic, motile microorganisms through a porous medium on a rotating disk. Khan et al. [26] investigated axisymmetric flow generated by a nanofluid with moving microorganisms on a porous moving disk without mass flux. Shahid et al. [27] numerically studied the interaction of floating microorganisms in a slimy stream with nanoparticles over an inflated sheet. Hussain et al. [28] investigated the complex flow involving magnetically crossed convection when a porous medium is traversed by microorganisms and nanoparticles between two disks. Alzahrani et al. [29] analyzed the impact of Hall current and moving microorganisms on nanofluid flow induced by disk rotation under varying slip and radiative heat conditions. Khan et al. [30] numerically studied an enhanced model incorporating bioconvective processes, gyrotactic motile microorganisms, and magnetohydrodynamics. Chu et al. [31] examined bio-convection involving non-Newtonian and Jeffery nanofluid with motile microorganisms across aligned disks, considering heat radiation and wobbly thrust streams. In the study by Khan et al. [32], the impact of entropy generation was analyzed in

unsteady magneto bioconvective Casson fluid flow with microorganisms, accounting for Cattaneo–Christov heat and mass flux theory. Bég et al. [33] proposed a mathematical concept for continuous connective von-Karman whirling flow from a porous, radially extended, airtight disk immersed in a nanofluid-doped Darcy medium with mobile microorganisms. Khan et al. [34] scrutinized the impact of bioconvection due to microorganisms on Buongiorno nanofluid modulation, considering the Cattaneo-Christov thermal flux theory. They also explored Oldroyd-B nanofluid behavior and gyrotactic microorganisms in a rotating system under the influence of Hall current and Darcy porous medium effects.

Magnetohydrodynamic (MHD) flows through porous media and holds significant practical applications, especially in the context of MHD convective fluxes and heat transfer. This relevance is underscored in the MHD system design. When combined with viscous dissipation, a viscous fluid with elastic properties, subject to applied stress, stores energy in the form of strain energy. Comparatively, a viscous fluid with inelastic properties emphasizes strain rate overstrain, in contrast to elastic fluids, where even minimal strain is significant due to its potential to restore the original shape. Only viscous fluids with elastic properties can partially regain shape after tension release; other fluids retain the entire strain. Shoaib et al. [35] delved into heat and mass transport mechanisms in the flow of a hybrid nanofluid (HNF) over an MHD active circular disk. Chaudhary et al. [36] investigated (TiO<sub>2</sub>-CuO/EG) HNF flow, examining 2D radial symmetry and MHD stillness point movement over a radially driven disk. Vijay et al. [37] studied the MHD flow of a hybrid nanofluid over a slowly spinning disk with considerations of Ohmic heating, Soret and Dufour effects. Analytical analysis of two-dimensional magnetohydrodynamic hybrid nanofluid flow incorporating Hall and ion-slip effects was conducted by Khan et al. [38]. Nabil et al. [39] explored the continuous magneto-hydrodynamic flow of nanofluids caused by similarly spinning unbounded disks. Reddy et al. [40] investigated MHD boundary layer flow, along with the mass and heat transmission properties of copper-water and Silver-water nanofluids across a spinning disk placed on a porous medium containing thermal radiation and chemical reactions. Vajravelu et al. [41] examined the effects of irregular stream characteristics, velocity lapse, and temperature lapse on the MHD flow of nanofluids across two aligned disks. Khan et al. [42] elaborated on Hall current effects, Arrhenius activation energy, and binary chemical reactions in the rotating flow of hybrid nanofluids between double disks. The impact of velocity and temperature slip on the squeezing MHD flow of nanofluids across aligned disks was reviewed by Mohyud-Din et al. [43]. Ouyang et al. [44] demonstrated thermal and mass transport in a three-dimensional hybrid nanofluid (HNF) flow across a spinning disk under the influence of a non-changing magnetic force acting counter to the flow direction. Tassaddiq et al. [10] explored the flow of an immiscible HNF over an impermeable spinning plate, accounting for magnetic field influence. Yahaya et al. [45] analyzed the Al<sub>2</sub>O<sub>3</sub>-Cu/H<sub>2</sub>O (HNF) behavior over a stellate force disk using a magnetic field, viscous-Ohmic dissipation, and convective boundary conditions. Khan et al. [46] addressed the mechanical characteristics of a rotating system involving double disks, considering the impact of Hall current, entropy generation, Arrhenius activation energy, and binary chemical reactions. Ramzan et al. [47] investigated the flow of a second-grade nanofluid alongside microorganism movement over a thin needle, accounting for dipole effects, entropy generation, and thermal radiation. Qureshi et al. [48] focus on investigating the thermal characteristics of viscous fluid flow between orthogonally rotating disks, incorporating metallic matrix nanocomposite and ceramic matrix nanocomposite materials into the analysis.

In recent times, the assessment of mass and heat transfer through porous media over curved shapes has gained significant importance. This significance arises from its wide-ranging applications in various fields such as the chemical industry, the manufacturing of smart heating/cooling devices, energy-efficient systems, and the nuclear process industry. Curved geometries such as cones, cylinders, spheres, disks, ellipses, wavy channels, and torus structures are common examples. The pursuit of energy-efficient devices has piqued the interest of researchers in the study of

flow over rotating disks. Applications like centrifugal pumps, spin coating, high-temperature fluid pumping, and turbo machinery fall under this domain. The mechanisms underlying mass and heat transfer in the three-dimensional radiative movement of a hybrid nanofluid (HNF) over a spinning disk were investigated by Shoaib et al. [49]. Ahmadian et al. [50] explored the heat and mass transfer of an unstable Ag-MgO (HNF) flow induced by the up-and-down motion of a wavy spinning disk. Alghamdi et al. [51] delved into the three-dimensional movement of thermal and mass transfer within a rotating disk influenced by activation energy and a magnetic field. Dinarvand et al. [52] conducted an analytical investigation using a revolving impermeable disk and a steady radial stretching rate to examine the immiscible unidirectional steady 3D flow across the boundary layer of a ZnO-Au HNF. Khan et al. [53] investigated the impact of Cattaneo-Christov thermal flux, Maxwell nanofluid, and gyrotactic phenomena on flow past a spinning disk. Reddy et al. [40] explored Copper-water and Silver-water nanofluids, studying MHD boundary layer flow, thermal transmission, and mass flow characteristics across a rotating disk placed in a porous medium, considering factors such as thermal radiation, chemical processes, and partial slip. Vajravelu et al. [41] studied the three-dimensional effects of mass and heat transfer in nanofluids between two parallel disks using transpiration, considering various fluid features, velocity slip, and temperature slip. Khan et al. [22] examined the impact of chemical reactions on the thermodynamics of second-grade nanofluids, accounting for the effects of magnetic fields and thermal radiation. Abdelmalek et al. [54] explored the potential of combining metallic and metallic-oxides nanoparticles to create a novel hybrid material with unique properties. They developed an MHD-hybrid model for a thermal energy system using seven distinct types of nanoparticles. Qureshi et al. [55] delved into the idiosyncrasies of the cluster interfacial nanolayer theory within a thermal conductivity-centric model, concurrently scrutinizing the magnetohydrodynamic influence on the amalgamation of metallic oxide nanomaterials with the base fluid. Alanazi et al. [9] explored three-dimensional flow with hybrid nanofluids through swirling porous disks and an annular sector, utilizing diverse nanoparticle sizes and shapes in single-phase simulations, emphasizing thermophysical attributes.

In this work, motile microorganisms flow between two orthogonal motion permeable disks in a ternary hybrid MHD nanofluid is investigated to illustrate the phenomena of mass and heat transfer. The ternary hybrid nanofluid's thermophysical characteristics are influenced by the base fluid utilized, additional additives, form, size, concentrations, and volume fraction. The numerical values of heat transfer are calculated using two different ternary hybrid nanofluids on various shape factors, and the results are compared to ascertain which shape factor in a certain ternary HNF responds to a high rate of thermal transmission. This research aims to expand upon the recent study conducted by Kashif et al. [56]. It includes considerations of various factors, including unsteady flow, magnetic fields, the presence of motile microorganisms, the effect of shape and size factors, and their combined impact on the behavior of ternary hybrid nanofluids within the boundary layer. Thus, the results will be used in the accurate selection of shape factors in a particular ternary HNF to obtain the highest rate of thermal transmission. In the work, the dimensionless similarity transformation has been employed for converting the controlling 3D partial-differential equation (PDE) into ordinary differential equations (ODEs). In addition to the shooting technique, the Runge-Kutta integration method of the 4th order has been employed to formulate the mathematical formula of ODEs. In the following charts and graphs, the effects of multiple non-dimensional characteristics are examined and displayed.

## 2. Novelty

Trihybrid nanofluids can be used to enhance heat transfer efficiency in various thermal systems, such as heat exchangers, radiators, and cooling systems. It can also be employed in thermal energy storage systems to increase the energy storage capacity and improve the overall

performance of the system. By incorporating nanoparticles with high thermal conductivity, the rate of energy storage and release can be enhanced the solar thermal systems, trihybrid nanofluids can be utilized to improve the efficiency of solar collectors.

The expansion of the present study has been emphasized as

1. We used two types of ternary hybrid nanofluids with different nanoparticles.
2. We also considered the shape and size effects of nanoparticles.
3. We also incorporated the impacts of motile microorganisms.
4. Moreover, the two-dimensional case is extended to the three-dimensional problem.

### 2.1. Mathematical formulation

The paper investigates the flow of a trihybrid MHD nanofluid between two orthogonal permeable disks. The study considers a three-dimensional, time-dependent, immiscible flow involving heat and mass transfer. The impact of an external magnetic force, when applied along the  $z$ -axis, is neglected due to the significantly low Reynolds number values. One of the permeable disks, with a diameter of  $2r$ , experiences oscillations along the vertical axis. The velocity field is defined in the cylindrical coordinate system as  $v = (u(r, z, t), v(r, z, t), w(r, z, t))$ , as outlined in the physical model. The paper provides Table 1, which presents the thermophysical properties of the trihybrid nanofluid, and Table 2, illustrating the properties of the base fluid and various nanoparticles. In the context of the study,  $T_1$ ,  $C_1$ , and  $N_1$  refer to the characteristics associated with the fluid flow near the lower porous disk, including temperature, concentration, and motile microorganisms. Correspondingly,  $T_2$ ,  $C_2$ , and  $N_2$  represent the attributes of the fluid flow near the upper-porous disk. These variables are depicted in Figure 1. The governing equations are formulated based on the assumptions presented in reference [23], as follows:

$$\frac{\partial u}{\partial r} + \frac{u}{r} + \frac{\partial w}{\partial z} = 0 \tag{1}$$

$$\frac{\partial u}{\partial t} + u \frac{\partial u}{\partial r} + w \frac{\partial u}{\partial z} - \frac{v^2}{r} = -\frac{1}{\rho_{trihnf}} \frac{\partial p}{\partial r} + \nu_{trihnf} \left( \frac{\partial^2 u}{\partial r^2} + \frac{1}{r} \frac{\partial u}{\partial r} - \frac{u}{r^2} + \frac{\partial^2 u}{\partial z^2} \right) - \frac{\sigma_e B_0^2}{\rho_{trihnf}} u \tag{2}$$

**Table 1.** Thermophysical properties of tri-hybrid nanofluid [2, 57].

Properties	(HNFDs)
Density ( $\rho$ )	$\rho_{trihnf} = \varphi_1 \rho_{s_1} + \varphi_2 \rho_{s_2} + \varphi_3 \rho_{s_3} - (1 - \varphi_1 - \varphi_2 - \varphi_3) \rho_{bf}$
Viscosity ( $\mu$ )	$\mu_{trihnf} = \frac{\mu_{bf}}{(1 - (\varphi_1 + \varphi_2 + \varphi_3))^{2.5}}$
Heat capacity ( $\rho C_p$ )	$(\rho C_p)_{trihnf} = \varphi_1 (\rho C_p)_{s_1} + \varphi_2 (\rho C_p)_{s_2} + \varphi_3 (\rho C_p)_{s_3} + (1 - \varphi_1 - \varphi_2 - \varphi_3) (\rho C_p)_{bf}$
Thermal conductivity (K)	$k_{trihnf} = \frac{k_{s3} + (n_3 - 1)k_{hnf} - (n_3 - 1)\varphi_3(k_{hnf} - k_{s3})}{k_{s3} + (n_3 - 1)k_{hnf} + \varphi_3(k_{hnf} - k_{s3})} k_{hnf}$ $k_{hnf} = \frac{k_{s2} + (n_2 - 1)k_{nf} - (n_2 - 1)\varphi_2(k_{nf} - k_{s2})}{k_{s2} + (n_2 - 1)k_{nf} + \varphi_2(k_{nf} - k_{s2})} k_{nf}$ Where $k_{nf} = \frac{k_{s1} + (n_1 - 1)k_{bf} - (n_1 - 1)\varphi_1(k_{bf} - k_{s1})}{k_{s1} + (n_1 - 1)k_{bf} + \varphi_1(k_{bf} - k_{s1})} k_{bf}$

**Table 2.** Properties of base fluids and NPs [58].

Base fluid/NPs	$\rho$ ( kg m <sup>-3</sup> )	$C_p$ ( J k g <sup>-1</sup> k <sup>-1</sup> )	$\kappa$ (wm <sup>-1</sup> k <sup>-1</sup> )
H <sub>2</sub> O	997.1	4179	0.613
Cu	8933	385	401
Al <sub>2</sub> O <sub>3</sub>	3970	765	40
Fe <sub>3</sub> O <sub>4</sub>	5180	670	9.7
TiO <sub>2</sub>	4250	686.2	8.9538

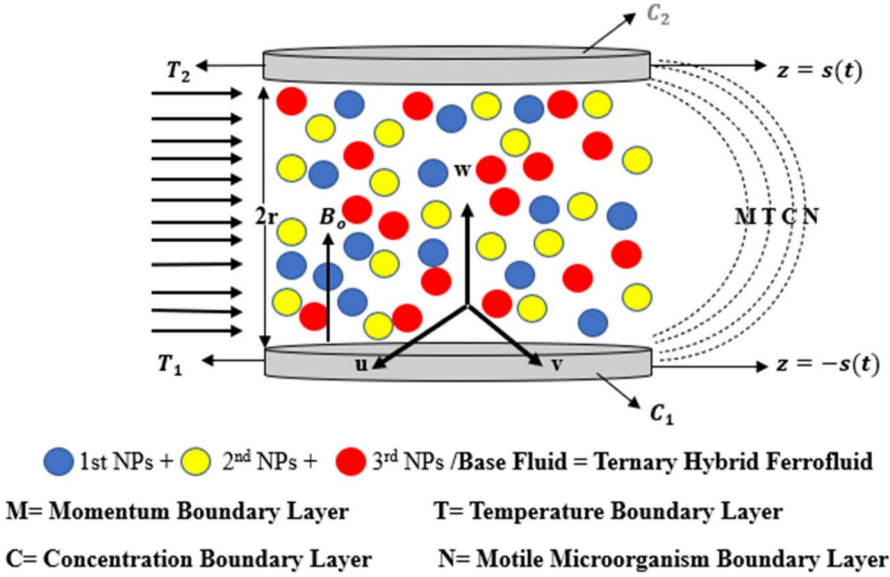


Figure 1. Physical model.

$$\frac{\partial v}{\partial t} + u \frac{\partial v}{\partial r} + w \frac{\partial v}{\partial z} + \frac{uv}{r} = v_{trihnf} \left( \frac{\partial^2 v}{\partial r^2} + \frac{1}{r} \frac{\partial v}{\partial r} - \frac{v}{r^2} + \frac{\partial^2 v}{\partial z^2} \right) - \frac{\sigma_e B_0^2}{\rho_{trihnf}} v \quad (3)$$

$$\frac{\partial w}{\partial t} + u \frac{\partial w}{\partial r} + w \frac{\partial w}{\partial z} = -\frac{1}{\rho_{trihnf}} \frac{\partial p}{\partial z} + v_{hnf} \left( \frac{\partial^2 w}{\partial r^2} + \frac{1}{r} \frac{\partial w}{\partial r} + \frac{\partial^2 w}{\partial z^2} \right) \quad (4)$$

$$\frac{\partial T}{\partial t} + u \frac{\partial T}{\partial r} + w \frac{\partial T}{\partial z} = \alpha_{trihnf} \frac{\partial^2 T}{\partial z^2} \quad (5)$$

$$\frac{\partial C}{\partial t} + u \frac{\partial C}{\partial r} + w \frac{\partial C}{\partial z} = (D_b)_{trihnf} \frac{\partial^2 C}{\partial z^2} \quad (6)$$

$$\frac{\partial N}{\partial t} + u \frac{\partial N}{\partial r} + w \frac{\partial N}{\partial z} + \frac{bW_c}{C_1 - C_2} \frac{\partial}{\partial z} \left( N \frac{\partial C}{\partial z} \right) = (D_n)_{trihnf} \frac{\partial^2 N}{\partial z^2} \quad (7)$$

where  $\sigma_e$  is the electrical conductivity,  $W_c$  is represented by cell swimming velocity,  $B_0^2$  stands for the strong magnetic field,  $N$  represents the density of motile microorganisms,  $p$ , and  $T$  are the pressure and temperature terms,  $\alpha_{trihnf}$ ,  $\rho_{trihnf}$ , and  $v_{trihnf}$  show that the thermal diffusivity, density, or kinematics viscosity of the tri-hybrid nanofluids, respectively,  $(D_b)_{trihnf}$ ,  $(D_n)_{trihnf}$  show the mass diffusivity and motile density of tri hybrid nanofluid, respectively.

The flow situation for boundary conditions is:

$$\begin{aligned} z_1 = -s(t) \quad u = 0 \quad v = -\frac{rA_1 s'(t)}{2s} \quad w = -A_1 s'(t) \quad T = T_1 \quad C = C_1 \quad N = N_1 \quad \text{and} \\ z_1 = s(t) \quad u = 0 \quad v = \frac{rA_1 s'(t)}{2s} \quad w = A_1 s'(t) \quad T = T_2 \quad C = C_2 \quad N = N_2 \end{aligned} \quad (8)$$

The  $s'(t)$  dash here represents the derivative concerning time  $t$ , and  $A_1$  seems to be the partition penetrability measure.

Here are the similarity factors that we introduce to get rid of the pressure term:

$$\eta = \frac{z}{s} u = -\frac{rv_f}{s^2} F_\eta(\eta, t), \quad v = \frac{rv_f}{s^2} G(\eta, t), \quad w = \frac{2v_f}{s} F(\eta, t) \quad \theta = \frac{T - T_2}{T_1 - T_2}, \tag{9}$$

$$\chi(\eta) = \frac{C - C_2}{C_1 - C_2}, \quad \psi(\eta) = \frac{N - N_2}{N_1 - N_2}$$

which resulted in:

$$\frac{v_{trihnf}}{v_f} F_{\eta\eta\eta\eta} + \alpha(3F_{\eta\eta} + \eta F_{\eta\eta\eta}) - 2FF_{\eta\eta\eta} - \frac{s^2}{v_f} F_{\eta\eta t} + 2GG_\eta - \frac{\rho_f}{\rho_{trihnf}} MF_{\eta\eta} = 0 \tag{10}$$

$$\frac{v_{trihnf}}{v_f} G_{\eta\eta} + \alpha(2G + \eta F_\eta) + 2GF_\eta - \frac{s^2}{v_f} G_t - 2FG_\eta - \frac{\rho_f}{\rho_{trihnf}} MG = 0 \tag{11}$$

$$\theta_{\eta\eta} + \frac{v_f}{\alpha_{trihnf}} (\alpha\eta - 2F)\theta_\eta - \frac{k^2}{\alpha_{nf}} \theta_t = 0 \tag{12}$$

$$(D_b)_{trihnf} \chi'' + v_f(\alpha\eta - 2F)\chi' - k^2 \chi_t = 0 \tag{13}$$

$$(D_n)_{trihnf} \psi'' + v_f(\alpha\eta - 2F)\psi' - k^2 \psi_t - bW_c(\psi'\chi' + \psi''\chi + N_2\chi'') = 0 \tag{14}$$

combined with the following boundary conditions:

$$\eta = -1, \quad F = -Re, \quad F_\eta = 0, \quad G = -Re, \quad \theta = 1, \quad \chi = 1, \quad \psi = 1$$

$$\text{and } \eta = 1, \quad F = Re, \quad F_\eta = 0, \quad G = Re, \quad \theta = 0, \quad \chi = 0, \quad \psi = 0 \tag{15}$$

Here  $\alpha = \frac{ss'(t)}{v_f}$  demonstrates the wall expansion ratio,  $Re = \frac{A_1 ss'(t)}{2v_f}$  is the permeable Reynolds number,  $v_{trihnf} = \frac{\mu_{trihnf}}{\rho_{trihnf}}$  stands for the viscosity of tri-hybrid nanofluid,  $\alpha_{trihnf} = \frac{k_{trihnf}}{(\rho c_p)_{trihnf}}$  illustrates the tri hybrid nanofluid's thermal diffusivity,  $\gamma = \frac{N_2}{N_2 - N_1}$  denote density's ratio for the motile microorganisms over the disk,  $Pr = \frac{(\mu c_p)_f}{k_f}$  denoted the Prandtl number,  $Sc = \frac{v_f}{(D_{b,n})_{trihnf}}$  represent the Schmidt number,  $Pe = \frac{bW_c}{(D_n)_{trihnf}}$  is denoted by Peclet number and  $M = \frac{\sigma_e B_0^2 s^2}{\mu_f}$  is the magnetic parameter. In which the tri-hybrid nanofluids' influence on thermal conductivity is  $k_{trihnf}$  and the specific capacitance of (THNFs) is  $(\rho c_p)_{trihnf}$ .

Consequently, we put  $F = f Re$ ,  $G = g Re$  and use the instance after Majdalani et al. [59] where  $\alpha$  proves to be a constant,  $f = f(\eta)$ ,  $\theta = \theta(\eta)$ ,  $\chi = \chi(\eta)$ , and  $\psi = \psi(\eta)$ , that results in  $\theta_t = 0$ ,  $g_{\eta t} = 0$ ,  $f_{\eta t} = 0$ ,  $\chi_t = 0$  and  $\psi_t = 0$ . Consequently, we obtain the following equations:

$$\frac{v_{trihnf}}{v_f} f_{\eta\eta\eta\eta} + \alpha(3f_{\eta\eta} + \eta f_{\eta\eta\eta}) - 2ff_{\eta\eta\eta} + 2Regg_\eta - \frac{\rho_f}{\rho_{trihnf}} Mf_{\eta\eta} = 0 \tag{16}$$

$$\frac{v_{trihnf}}{v_f} g_{\eta\eta} + \alpha(2g + \eta g_\eta) + 2Re(gf_\eta - fg_\eta) - \frac{\rho_f}{\rho_{trihnf}} Mg = 0 \tag{17}$$

$$\theta_{\eta\eta} + \frac{v_f}{\alpha_{trihnf}} Pr(\alpha\eta - 2fRe)\theta_\eta = 0 \tag{18}$$

$$\chi'' + Sc(\alpha\eta - 2fRe)\chi' = 0 \tag{19}$$

$$\psi'' + Sc(\alpha\eta - 2fRe)\psi' - Pe(\psi'\chi' + \psi''\chi + N_2\chi'') = 0 \tag{20}$$

$$\eta = -1; \quad f = -1, \quad f_\eta = 0, \quad g = -1, \quad \theta = 1, \quad \chi = 1, \quad \psi = 1$$

$$\text{and } \eta = 1; \quad f = 1, \quad f_\eta = 0, \quad g = 1, \quad \theta = 0, \quad \chi = 0, \quad \psi = 0. \tag{21}$$

### 3. Practical and engineering interest

Physical properties like skin friction, Nusselt number, Sherwood number, and motile number are necessary for industrial engineering instances to build nanoscale machinery. On both porous disks, each of the above factors has been considered in calculations.

#### 3.1. Skin friction coefficients

Top and bottom porous disk skin friction show that the  $C_{f1}$  and  $C_{f-1}$  which are expressed as:

$$C_{f-1} = \frac{\xi_w|_{\eta = -1}}{\rho_{bf}(s'A_1)^2} = \frac{1}{Re_r(1 - \varphi_1 - \varphi_2 - \varphi_3)^{2.5}} \sqrt{(f''(-1))^2 + (g'(-1))^2} \quad (22)$$

$$C_{f1} = \frac{\xi_w|_{\eta = 1}}{\rho_{bf}(s'A_1)^2} = \frac{1}{Re_r(1 - \varphi_1 - \varphi_2 - \varphi_3)^{2.5}} \sqrt{(f''(1))^2 + (g'(1))^2}$$

The local Reynolds number is denoted by  $Re_r = 4\left(\frac{\xi}{r}\right)\left(\frac{1}{(Re)^2}\right)$  and the total shear stress stands for  $\xi_w$ . The total shear stress is defined as  $\xi_w = \sqrt{\xi_{zr}^2 + \xi_{\theta z}^2}$ . The flow of upper and lower porous disks is expressed in the radial and tangential direction represented as  $\xi_{rz}$  and  $\xi_{\theta z}$ , respectively,

$$\xi_{zr} = \mu_{trihnf} \left(\frac{\partial u}{\partial z}\right) \Big|_{\eta = -1} = \frac{\mu_{bf}}{(1 - \varphi_1 - \varphi_2 - \varphi_3)^{2.5}} \left(\frac{rv_f}{s^3}\right) f''(-1), \quad \text{and} \quad \xi_{\theta z} = \mu_{trihnf} \left(\frac{\partial v}{\partial z}\right) \Big|_{\eta = -1} = \frac{\mu_{bf}}{(1 - \varphi_1 - \varphi_2 - \varphi_3)^{2.5}} \left(\frac{rv_f}{s^3}\right) g'(-1).$$

#### 3.2. Nusselt numbers

$Nu_{z-1}$  and  $Nu_{z1}$  are thermal transmission flow (Nusselt number) for top and bottom porous disks, and are represented as

$$Nu_{z-1} = \frac{se_z}{\kappa_f(T_1 - T_2)} \Big|_{\eta = -1} = -\frac{k_{trihnf}}{\kappa_f} \theta'(-1), \quad (23)$$

$$Nu_{z1} = \frac{se_z}{\kappa_f(T_1 - T_2)} \Big|_{\eta = 1} = -\frac{k_{trihnf}}{\kappa_f} \theta'(1).$$

where  $e_z$  stand for heat flux which follows as:

$$e_z \Big|_{\eta = -1} = -k_{trihnf} \left(\frac{\partial T}{\partial z}\right) \Big|_{\eta = -1} = -\frac{(T_1 - T_2)}{s} k_{trihnf} \theta'(-1)$$

$$e_z \Big|_{\eta = 1} = -k_{trihnf} \left(\frac{\partial T}{\partial z}\right) \Big|_{\eta = 1} = -\frac{(T_1 - T_2)}{s} k_{trihnf} \theta'(1)$$

where  $Re = \frac{A_1 s s'(t)}{2v_f}$ .

#### 3.3. Sherwood number

The flow ratio between conventional mass transmission over the mass transmission of diffusion is called the Sherwood number. The rate of flow of mass transmission across the upper and lower porous disks (Sherwood number) denoted by  $Sh|_{\eta = -1}$  and  $Sh|_{\eta = 1}$  have the following mathematical expressions,

$$\begin{aligned}
 Sh|_{\eta = -1} &= \frac{kq_z}{(D_b)_{trihnf}(C_1 - C_2)}|_{\eta = -1} = -\chi'(-1) \\
 Sh|_{\eta = 1} &= \frac{kq_z}{(D_b)_{trihnf}(C_1 - C_2)}|_{\eta = 1} = -\chi'(1)
 \end{aligned}
 \tag{24}$$

Here:  $q_z|_{\eta = -1} = -(D_b)_{trihnf} \left( \frac{\partial C}{\partial z} \right) |_{\eta = -1} = -(D_b)_{trihnf} \frac{(C_1 - C_2)}{k} \chi'(-1)$ ,  $q_z|_{\eta = 1} = -(D_b)_{trihnf} \left( \frac{\partial C}{\partial z} \right) |_{\eta = 1} = -(D_b)_{trihnf} \frac{(C_1 - C_2)}{k} \chi'(1)$ , where  $Re = \frac{A_1 s'(t)}{2\nu_f}$ .

**3.4. Motile density number**

Both porous disks are represented by  $Nn|_{\eta = -1}$  and  $Nn|_{\eta = 1}$  of motile number and are expressed as:

$$\begin{aligned}
 Nn|_{\eta = -1} &= \frac{kq_n}{(D_n)_{trihnf}(N_1 - N_2)}|_{\eta = -1} = -\psi'(-1) \\
 Nn|_{\eta = 1} &= \frac{kq_n}{(D_n)_{trihnf}(N_1 - N_2)}|_{\eta = 1} = -\psi'(1) \\
 q_z|_{\eta = -1} &= -(D_n)_{trihnf} \left( \frac{\partial N}{\partial z} \right) |_{\eta = -1} = -(D_n)_{trihnf} \frac{(N_1 - N_2)}{k} \psi'(-1) \\
 q_z|_{\eta = 1} &= -(D_n)_{trihnf} \left( \frac{\partial N}{\partial z} \right) |_{\eta = 1} = -(D_n)_{trihnf} \frac{(N_1 - N_2)}{k} \psi'(1)
 \end{aligned}
 \tag{25}$$

**3.5. Numerical solution and modeling for thermophysical properties of tri hybrid nanofluid**

To transform the non-linear PDE into a pair of linked systems ODE having extremely nonlinear properties, form Eqs. (16), (17), (18), (19), and (20).

$$\begin{aligned}
 &\left( \frac{1}{(1 - (\varphi_1 + \varphi_2 + \varphi_3))^{2.5} \left( (1 - \varphi_1 - \varphi_2 - \varphi_3) + \varphi_1 \left( \frac{\rho_{s1}}{\rho_{bf}} \right) + \varphi_2 \left( \frac{\rho_{s2}}{\rho_{bf}} \right) + (\varphi_3) \left( \frac{\rho_{s3}}{\rho_{bf}} \right) \right)} \right) f''''[\eta] \\
 &- \alpha(3f''[\eta] + \eta f''[\eta]) - 2Ref[\eta]f''[\eta] + 2Reg[\eta]g'[\eta] \\
 &- \left( \frac{1}{\left( (1 - \varphi_1 - \varphi_2 - \varphi_3) + \varphi_1 \left( \frac{\rho_{s1}}{\rho_{bf}} \right) + \varphi_2 \left( \frac{\rho_{s2}}{\rho_{bf}} \right) + (\varphi_3) \left( \frac{\rho_{s3}}{\rho_{bf}} \right) \right)} \right) M f''[\eta] = 0
 \end{aligned}
 \tag{26}$$

$$\begin{aligned}
 &\left( \frac{1}{(1 - (\varphi_1 + \varphi_2 + \varphi_3))^{2.5} \left( (1 - \varphi_1 - \varphi_2 - \varphi_3) + \varphi_1 \left( \frac{\rho_{s1}}{\rho_{bf}} \right) + \varphi_2 \left( \frac{\rho_{s2}}{\rho_{bf}} \right) + (\varphi_3) \left( \frac{\rho_{s3}}{\rho_{bf}} \right) \right)} \right) g''[\eta] \\
 &+ \alpha(2g[\eta] + \eta g'[\eta]) + 2Re(g[\eta]f'[\eta] - f[\eta]g'[\eta]) \\
 &- \left( \frac{1}{\left( (1 - (\varphi_1 + \varphi_2 + \varphi_3)) + (\varphi_1) \left( \frac{\rho_{s1}}{\rho_{bf}} \right) + (\varphi_2) \left( \frac{\rho_{s2}}{\rho_{bf}} \right) + (\varphi_3) \left( \frac{\rho_{s3}}{\rho_{bf}} \right) \right)} \right) Mg[\eta] = 0
 \end{aligned}
 \tag{27}$$

$$\theta''[\eta] + \left( (1 - (\varphi_1 + \varphi_2 + \varphi_3)) + (\varphi_1) \left( \frac{\rho_{cps_1}}{\rho_{cpbf}} \right) + (\varphi_2) \left( \frac{\rho_{cps_2}}{\rho_{cpbf}} \right) + (\varphi_3) \left( \frac{\rho_{cps_3}}{\rho_{cpbf}} \right) \right) \left( \frac{k_{s_3} + (n_3 - 1)k_{hnf} + \varphi_3(k_{hnf} - k_{s_3})}{k_{s_3} + (n_3 - 1)k_{hnf} - (n_3 - 1)\varphi_3(k_{hnf} - k_{s_3})} \right) \left( \frac{k_{s_2} + (n_2 - 1)k_{nf} + \varphi_2(k_{mbf} - k_{s_2})}{k_{s_2} + (n_2 - 1)k_{nf} - (n_2 - 1)\varphi_2(k_{nf} - k_{s_2})} \right) \left( \frac{k_{s_1} + (n_1 - 1)k_{bf} + \varphi_1(k_{bf} - k_{s_1})}{k_{s_1} + (n_1 - 1)k_{bf} - (n_1 - 1)\varphi_1(k_{bf} - k_{s_1})} \right) Pr(\alpha\eta - 2Re_f[\eta])\theta'[\eta] = 0 \quad (28)$$

$$\chi''[\eta] + Sc(\alpha\eta - 2fRe)\chi'[\eta] = 0 \quad (29)$$

$$\psi''[\eta] + Sc(\alpha\eta - 2f[\eta]Re)\psi'[\eta] - Pe(\psi'[\eta]\chi'[\eta] + \psi''[\eta]\chi[\eta] + N_2\chi''[\eta]) = 0 \quad (30)$$

Here:

$$L_1 = \left( \frac{1}{(1 - (\varphi_1 + \varphi_2 + \varphi_3))^{2.5} \left( (1 - \varphi_1 - \varphi_2 - \varphi_3) + \varphi_1 \left( \frac{\rho_{s_1}}{\rho_{bf}} \right) + \varphi_2 \left( \frac{\rho_{s_2}}{\rho_{bf}} \right) + (\varphi_3) \left( \frac{\rho_{s_3}}{\rho_{bf}} \right) \right)} \right) \quad (31)$$

$$L_2 = \left( \frac{1}{\left( (1 - \varphi_1 - \varphi_2 - \varphi_3) + \varphi_1 \left( \frac{\rho_{s_1}}{\rho_{bf}} \right) + \varphi_2 \left( \frac{\rho_{s_2}}{\rho_{bf}} \right) + (\varphi_3) \left( \frac{\rho_{s_3}}{\rho_{bf}} \right) \right)} \right) \quad (32)$$

$$L_3 = \left( (1 - \varphi_1 - \varphi_2 - \varphi_3) + \varphi_1 \left( \frac{\rho_{s_1}}{\rho_{bf}} \right) + \varphi_2 \left( \frac{\rho_{s_2}}{\rho_{bf}} \right) + (\varphi_3) \left( \frac{\rho_{s_3}}{\rho_{bf}} \right) \right) \quad (33)$$

$$D_1 = \left( \frac{k_{s_3} + (n_3 - 1)k_{hnf} + \varphi_3(k_{hnf} - k_{s_3})}{k_{s_3} + (n_3 - 1)k_{hnf} - (n_3 - 1)\varphi_3(k_{hnf} - k_{s_3})} \right) \quad (34)$$

$$D_2 = \left( \frac{k_{s_2} + (n_2 - 1)k_{nf} + \varphi_2(k_{nf} - k_{s_2})}{k_{s_2} + (n_2 - 1)k_{nf} - (n_2 - 1)\varphi_2(k_{nf} - k_{s_2})} \right) \quad (35)$$

$$D_3 = \left( \frac{k_{s_1} + (n_1 - 1)k_{bf} + \varphi_1(k_{bf} - k_{s_1})}{k_{s_1} + (n_1 - 1)k_{bf} - (n_1 - 1)\varphi_1(k_{bf} - k_{s_1})} \right) \quad (36)$$

$$\omega = D_1 D_2 D_3 \quad (37)$$

Putting values of (30–35), and (36) in Eqs. (26–29) and (30) or final result are:

$$L_1 f''''[\eta] - \alpha(3f''[\eta] + \eta f''[\eta]) - 2Re_f[\eta] f''[\eta] - L_2 M f''[\eta] = 0 \quad (38)$$

$$L_1 g''[\eta] + \alpha(2g[\eta] + \eta g'[\eta]) + 2Re(g[\eta]f'[\eta] - f[\eta]g'[\eta]) - L_2 M g[\eta] = 0 \quad (39)$$

$$\theta''[\eta] + L_3 \omega Pr(\alpha\eta - 2Re_f[\eta])\theta'[\eta] = 0 \quad (40)$$

$$\chi''[\eta] + Sc(\alpha\eta - 2Re_f[\eta])\chi'[\eta] = 0 \quad (41)$$

$$\psi''[\eta] + Sc(\alpha\eta - 2f[\eta]Re)\psi'[\eta] - Pe(\psi'[\eta]\chi'[\eta] + \psi''[\eta]\chi[\eta] + N_2\chi''[\eta]) = 0 \quad (42)$$

### 3.6. Solution of the problem

We used the 4<sup>th</sup>-order RK numerical scheme together with the shooting technique to resolve the current flow scenario. To begin the procedure, the mentioned modification must be made:

$$\begin{aligned} j_1^* &= f[\eta], j_2^* = f'[\eta], j_3^* = f''[\eta], j_4^* = f'''[\eta], j_5^* = g[\eta], j_6^* = g'[\eta], j_7^* = \theta[\eta], j_8^* = \theta'[\eta], j_9^* \\ &= \chi[\eta], j_{10}^* = \chi'[\eta], j_{11}^* = \psi[\eta], j_{12}^* = \psi'[\eta] \end{aligned} \quad (43)$$

To finish, the model is being altered as given in Eqs. (38), (39), (40), (41), and (42) below (42).

$$f''''[\eta] = \frac{1}{H_1} (\alpha(3f''[\eta] + \eta f'''\prime[\eta]) + 2Re f[\eta] f'''\prime[\eta] + H_2 M f''[\eta]) \quad (44)$$

$$g''[\eta] = \frac{1}{L_1} (-\alpha(2g[\eta] + \eta g'[\eta]) - 2Re(g[\eta] f'[\eta] + f[\eta] g'[\eta]) + L_2 M g[\eta]) \quad (45)$$

$$\theta''[\eta] = L_3 \omega Pr(-\alpha \eta + 2Re f[\eta]) \theta'[\eta] \quad (46)$$

$$\chi''[\eta] = Sc(-\alpha \eta + 2Re f[\eta]) \chi'[\eta] \quad (47)$$

$$\psi'' = Sc(-\alpha \eta + 2fRe) \psi' + Pe(\psi' \chi' + \psi'' \chi + N_2 \chi'') \quad (48)$$

By using the substitution in Eq. (43), the corresponding system is generated:

$$\begin{bmatrix} j_1^{*'} \\ j_2^{*'} \\ j_3^{*'} \\ j_4^{*'} \\ j_5^{*'} \\ j_6^{*'} \\ j_7^{*'} \\ j_8^{*'} \\ j_9^{*'} \\ j_{10}^{*'} \\ j_{11}^{*'} \\ j_{12}^{*'} \end{bmatrix} = \begin{bmatrix} j_2^* \\ j_3^* \\ j_4^* \\ \frac{1}{L_1} (\alpha(3j_3^* + \eta j_4^*) + 2Re j_1^* j_3^* + L_2 M j_3^*) \\ j_6^* \\ \frac{1}{L_1} (-\alpha(2j_5^* + \eta j_6^*) - 2Re(j_5^* j_2^* + j_1^* j_6^*) + L_2 M q_5^*) \\ j_8^* \\ L_3 \omega Pr(-\alpha \eta + 2Re f[\eta]) q_8^* \\ j_{10}^* \\ Sc(-\alpha \eta + 2Re j_1^*) j_9^* \\ j_{11}^* \\ Sc(-\alpha \eta + 2j_1^* Re) j_{11}^* + Pe(j_{11}^* j_{10}^* + \psi'' j_9^* + N_2 \chi'') \end{bmatrix} \quad (49)$$

Consequently, the initial condition is:

$$\begin{bmatrix} j_1^* \\ j_2^* \\ j_3^* \\ j_4^* \\ j_5^* \\ j_6^* \\ j_7^* \\ j_8^* \\ j_9^* \\ j_{10}^* \\ j_{11}^* \\ j_{12}^* \end{bmatrix} = \begin{bmatrix} -1 \\ 0 \\ 1 \\ 0 \\ -1 \\ 1 \\ 1 \\ 0 \\ 1 \\ 0 \\ 1 \\ 0 \end{bmatrix}$$

The problem is now solved using mathematics and a correct starting condition. Both the RK approach and the numerical “shooting method” were explored in this scenario. The computation of the necessary dimensionless ODEs is made easier by this method. To create the starting condition, we first use the shooting technique to make sure that the required level of accuracy is obtained, and the boundary criteria are fulfilled.

#### 4. Results and discussion

The final transformed Eqs. (26) through (30) are produced in this mathematical model research to build nonlinear boundary conditions. Since it is challenging to find an analytical expression for these kinds of equations, the Runge-Kutta technique is used as part of a numerical strategy to tackle the problem. Figure 1 displays the effects of associated physical variables on velocity, temperature, concentration, and motile microorganisms. These variables include the Peclet number, magnetic field, Prandtl number, Reynolds number, frictional volume, a ratio of density motile microorganisms, shape aspect, Schmidt number, as well as the expansion ratio parameter (2–10). The numerical effects of these physical parameters are shown in Tables 2–8. In Table 3, the comparison of two tri-hybrid nanofluids with different sizes, and shape factors are computed by changing the values of volume friction ( $\varphi_1$ ,  $\varphi_2$ , and  $\varphi_3$ ). The findings show that, among the four form parameters, the platelets possess high heat conductivity (sphere, bricks, cylindrical, and platelets). Additionally, the trihybrid nanofluid (Cu + Al<sub>2</sub>O<sub>3</sub>+Fe<sub>3</sub>O<sub>4</sub>/H<sub>2</sub>O) had greater thermal conductivity compared to the other tri-hybrid nanofluid (Cu + Al<sub>2</sub>O<sub>3</sub>+ TiO<sub>2</sub>/H<sub>2</sub>O) that was investigated. This computation is being done while increasing the value of volume friction from 1% to 4%.

In Table 4, the effects of a nondimensional parameter such as volume friction, expansion ratio, Reynolds number, and magnetic field parameter on tangential stress, shear stress, as well as the flow of thermal transmission under tri-hybrid nanofluid. In two separate tri-hybrid NFs (Cu + Al<sub>2</sub>O<sub>3</sub>+Fe<sub>3</sub>O<sub>4</sub>/H<sub>2</sub>O as well as Cu + Al<sub>2</sub>O<sub>3</sub>+ TiO<sub>2</sub>/H<sub>2</sub>O), these results are estimated. The findings demonstrate that the volume friction, as well as the magnetic field component in the tri-hybrid nanofluid (Cu + Al<sub>2</sub>O<sub>3</sub>+Fe<sub>3</sub>O<sub>4</sub>/H<sub>2</sub>O), vary inversely with heat transfer flow rate in the bottom porous disk, but effectively with shear stress as well as tangential stress. Holding the Reynolds value as well as the parameter of the magnetic field with fixed values, the expanding/contracting parameter ( $\alpha$ ) is changing inversely with shear stress, and tangential stress, as well as the heat transfer rate. While maintaining the expansion ratio parameter and the magnetic field parameter’s values unchanged, the Reynolds number (Re) fluctuates linearly with shear stress, tangential stress, and heat transfer rate. Physically, the Reynolds number plays a crucial role as an indicator of a fluid’s flow behavior, encompassing factors such as shear stress, tangential stress, and heat transfer rate. It tells us whether the dominant forces driving the flow are the inertial forces (associated with the fluid’s motion and velocity) or the viscous forces (related to the fluid’s resistance to flow). When the Reynolds number is less than 2000, the viscous forces dominate, resulting in laminar flow, where the fluid moves smoothly in well-defined layers. The values of shear stress and tangential stress simultaneously increased in the event of the parameter of magnetic force, but the values of heat transfer rate decreased. The trihybrid nanofluid (Cu + Al<sub>2</sub>O<sub>3</sub>+Fe<sub>3</sub>O<sub>4</sub>/H<sub>2</sub>O) has produced more precise numerical results when compared to the other two tri-hybrid NFs (Cu + Al<sub>2</sub>O<sub>3</sub>+ TiO<sub>2</sub>/H<sub>2</sub>O and Cu + Al<sub>2</sub>O<sub>3</sub>+ Fe<sub>3</sub>O<sub>4</sub>/H<sub>2</sub>O). The results presented in Table 5 reveal the impact of various factors on both mass transfer and the movement of motile microorganisms. Specifically, there is an observed increase in mass transfer and microorganism flow with positive increments in Schmidt number, Reynolds number, expansion ratio, Peclet number, and density ratio values, in total. Table 6 demonstrates the impact of the local Reynolds number ( $Re_r$ ), shape and size factors ( $n_1 = n_2 = n_3$ ), Schmidt number (Sc), and motile density parameters ( $N_2$ ) on the skin friction coefficient, Nusselt number, Sherwood

**Table 3.** Comparison of two tri-hybrid nanofluids with different types, sizes, and shape factors.

$\varphi_1 = \varphi_2 = \varphi_3$	Cu + Al <sub>2</sub> O <sub>3</sub> + TiO <sub>2</sub> /H <sub>2</sub> O				Cu + Al <sub>2</sub> O <sub>3</sub> +Fe <sub>3</sub> O <sub>4</sub> /H <sub>2</sub> O			
	Spherical (3)	Bricks (3.7)	Cylinders (4.9)	Plates (5.7)	Spherical (3)	Bricks (3.7)	Cylinders (4.9)	Plates (5.7)
	( $n_1=n_2=n_3$ )	( $n_1=n_2=n_3$ )	( $n_1=n_2=n_3$ )	( $n_1=n_2=n_3$ )	( $n_1=n_2=n_3$ )	( $n_1=n_2=n_3$ )	( $n_1=n_2=n_3$ )	( $n_1=n_2=n_3$ )
0.01 = 1%	0.01946	0.02072	0.02292	0.02439	0.019525	0.02078	0.022959	0.0244
0.02 = 2%	0.02652	0.02961	0.03512	0.03891	0.02668	0.02976	0.035236	0.03898
0.03 = 3%	0.03501	0.04048	0.05032	0.0571	0.0353	0.040763	0.050534	0.05726
0.04 = 4%	0.04492	0.05325	0.06818	0.07839	0.045392	0.053695	0.06852	0.07864

**Table 4.** Different nondimensional parameter effects on shear stress, tangential stress, and flow of heat transfer under tri-hybrid nanofluid.

$\varphi_1 = \varphi_2 = \varphi_3$	$\alpha$	Re	M	Cu + Al <sub>2</sub> O <sub>3</sub> + TiO <sub>2</sub> / H <sub>2</sub> O		Cu + Al <sub>2</sub> O <sub>3</sub> +Fe <sub>3</sub> O <sub>4</sub> / H <sub>2</sub> O			
				$ f'''[-1] $	$ g'[-1] $	$ \theta[-1] $	$ f'''[-1] $	$ g'[-1] $	$ \theta[-1] $
0.01	1	2	1	4.3181	0.01717	7.9841	4.339	0.033407	7.9862
0.02				4.4494	0.43078	6.8486	4.4997	0.5691	6.8518
0.03				4.567	0.8852	5.8844	4.6584	1.1586	5.8876
0.04				4.656	1.2804	5.0614	4.7995	1.7332	5.0628
	0.5			4.8008	1.6069	9.2480	4.8204	1.6024	9.2507
	0			5.3493	2.7605	10.5240	5.3729	2.7761	10.5278
	-0.5			5.9191	3.7077	11.8118	5.9478	3.7352	11.8154
	-1			6.4956	4.5378	13.106	6.5296	4.5738	13.1108
		1		3.0592	0.36321	2.7277	3.0599	0.3770	2.7267
		0		2.3657	0.28597	0.06573	2.3720	0.294	0.06578
		-1		2.0276	0.17971	0.00013	2.0335	0.1856	0.000129
		-3		1.882	0.11163	$1.45 \times 10^{-7}$	1.8867	0.116	$1.47 \times 10^{-7}$
			3	4.4287	1.0941	7.9822	4.4439	1.0727	7.9845
			5	4.584	1.8069	7.9787	4.5975	1.7982	7.9808
			7	4.7524	2.3346	7.9741	4.7647	2.3327	7.9766
			9	4.9217	2.752	7.9697	4.9337	2.7548	7.9721

**Table 5.** Numerical impact flow of mass transfer and motile microorganisms from different parameters.

Sc	Re	$\alpha$	Pe	$N_2$	$ \chi'[-1] $	$ \psi'[-1] $
1	1	1	0.5	2	0.77374	2.2454
3					1.5593	7.2403
5					2.5582	12.1914
7					3.6261	16.328
	2				1.4126	6.5826
	4				2.4119	9.7029
	6				5.4063	25.3163
			0.6		0.7737	3.0569
			0.7		0.7737	4.4797
			0.8		0.7737	7.4802
				4	0.77374	2.9397
				6	0.7737	3.6339
				8	0.7737	4.328

number, and motile numbers for the lower porous disk. Higher values of  $Re_r$  and Sc result in reduced flow for ternary hybrid nanofluids  $C_{f-1}$  and  $Sh_{z-1}$  in the lower disk. Conversely, increasing different  $n_1 = n_2 = n_3$  or  $N_2$  significantly enhances the flow of  $Nu_{z-1}$  and  $Nn_{z-1}$  in the bottom disk. Table 7 illustrates the differences between the outcomes of the previous study and our present investigation concerning the flow of heat transfer through a porous disk positioned below. Table 8 exhibits the refinement of our numerical solution with decreasing step sizes, instilling confidence in the soundness of our mathematical framework via convergence criteria, stability analysis, and meticulous control over numerical errors. Furthermore, our boundary conditions are met by symmetric and substantiated shear stress assessments at the lower and upper porous disks.

**Table 6.** Assessing the numerical influence of skin friction coefficient, Nusselt number, Sherwood number, and motile number for lower porous disks across various nondimensionalized parameters.

$Re_r$	$n_1=n_2=n_3$	$Sc$	$N_2$	$ C_{f-1} $	$ Nu_{z-1} $	$ Sh_{z-1} $	$ Nn_{z-1} $
1				2.2267	1.6641	0.52258	1.6409
1.5				2.0397	1.6641	0.52258	1.6409
2				1.6675	1.6641	0.52258	1.6409
	3			2.2267	1.6641	0.52304	1.6419
	3.7			2.2267	1.6698	0.52304	1.6419
	4.8			2.2267	1.6732	0.52304	1.6419
	5.7			2.2267	1.6785	0.52304	1.6419
		10		2.2267	1.5782	0.62257	1.5967
		12		2.2267	1.5782	0.54292	1.5967
		14		2.2267	1.5782	0.32346	1.5967
			1	2.2267	1.5782	0.62257	1.5967
			3	2.2267	1.5782	0.62257	1.7193
			5	2.2267	1.5782	0.62257	1.8419

**Table 7.** Comparing heat flow rates in the lower porous disk with fixed values of Prandtl number ( $Pr = 6.2$ ) and ( $\varphi_1 = \varphi_2 = \varphi_3 = 0.1$ ).

$Re$	Kashif et al [56]	Present results	Kashif et al. [56]	Present results
	$\alpha = 5$ $\theta(-1)$	$\alpha = 5$ $\theta(-1)$	$\alpha = -5$ $\theta(-1)$	$\alpha = -5$ $\theta(-1)$
-1	0.0057	0.0059	14.7353	14.7355
-3	0.1290	0.1292	9.9097	9.9099
-5	0.3975	0.3977	7.6396	7.6398
-7	0.7516	0.7518	6.8698	6.8701
-10	1.3717	1.3719	6.7262	6.7264

**Table 8.** Compute the convergence of our numerical solution across the range of lower to upper porous disks.

$\eta$	$f(\eta)$	$f'(\eta)$	$f''(\eta)$
-1	-1.	$5.421010862427522 \times 10^{-20}$	3.8263380603562362
-0.9	-0.9822731183403054	0.3413733024653446	3.0353232130042356
-0.8	-0.934048448994556	0.6128590374014543	2.4188535775182474
-0.7	-0.8615313293448681	0.829308480145765	1.9277918688881608
-0.6	-0.7696610507596361	1.0014323347742995	1.52749705589764
-0.5	-0.66246116818034	1.1369968146340375	1.1930864960901186
-0.4	-0.5432909182013186	1.2416321993493615	0.9063007011901943
-0.3	-0.4150295575993944	1.3193827622394538	0.6533890759789889
-0.2	-0.2802150831099695	1.3730800368373701	0.4236437575147292
-0.1	-0.1411521772630839	1.404591929113966	0.208350682623169
0	$-3.154850242159668 \times 10^{-9}$	1.4149809544537468	$-2.547479716584477 \times 10^{-8}$
0.1	0.1411521772630839	1.404591929113966	-0.208350682623169
0.2	0.2802150831099695	1.3730800368373701	-0.4236437575147292
0.3	0.4150295575993944	1.3193827622394538	-0.6533890759789889
0.4	0.5432909182013186	1.2416321993493615	0.9063007011901943
0.5	0.66246116818034	1.1369968146340375	1.1930864960901186
0.6	0.7696610507596361	1.0014323347742995	1.52749705589764
0.7	0.8615313293448681	0.829308480145765	1.9277918688881608
0.8	0.934048448994556	0.6128590374014543	2.4188535775182474
0.9	0.9822731183403054	0.3413733024653446	3.0353232130042356
1	1	$5.421010862427522 \times 10^{-20}$	3.8263380603562362

Figure 2 shows changes in the magnetic flux ( $M$ ) from  $-5$  to  $5$ . As  $M$  increases, two effects are observed. The first one is that the boundary layer's thickness near the porous disks grows due to the stronger magnetic flux. Secondly, despite this thickening, the flow speed in the central part of the flow decreases. This occurs because the magnetic field affects the flow dynamics near the surfaces, causing a slowdown in the central flow even though the boundary layer expands.

According to **Figure 3**, when the value of  $M$  shifts from  $-5$  to  $5$ , the momentum thickness of the boundary layer at the bottom of the porous disk increases. Notably, this increase persists as we transition to the more porous disk located in the middle of the wall.

The physical behavior inferred from this observation underscores that the fluid’s velocity is controlled by the transverse magnetic field, resulting in vibrational motion among the fluid’s particles. This vibrational motion primarily arises from the magnetic effect and is subject to modulation by the Lorentz force. **Figure 4** indicates that if the volume fraction ( $\varphi_1, \varphi_2, \varphi_3$ ) is increased then regarding the circulation of the ternary HNF ( $\text{Cu} + \text{Al}_2\text{O}_3 + \text{Fe}_3\text{O}_4/\text{H}_2\text{O}$ ), the border layer thickness of momentum is reduced within the radial velocity characteristic both for the upper and lower porous disks which are keeping other parameters ( $\alpha = -3, M = 2, Re = 2$ ) constant. **Figure 5** provides a physical interpretation of the significance of volume fraction values ( $\varphi_1, \varphi_2$ , and  $\varphi_3$ ) in the context of the flow of trihybrid nanofluids. It shows that as these volume fraction values increase, the momentum boundary layer thickness for the tangent velocity characteristic on the top porous disk also increases. This observation underscores the tangible impact of volume fractions on the flow dynamics within the system, indicating that higher

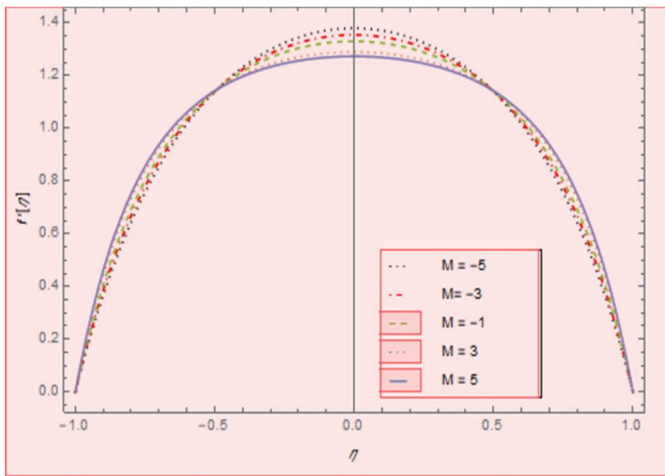


**Figure 2.** Magnetic field impact of radial velocity profile for  $\alpha = -1, \varphi_1 = \varphi_2 = \varphi_3 = 0.02, Re = 1$ .

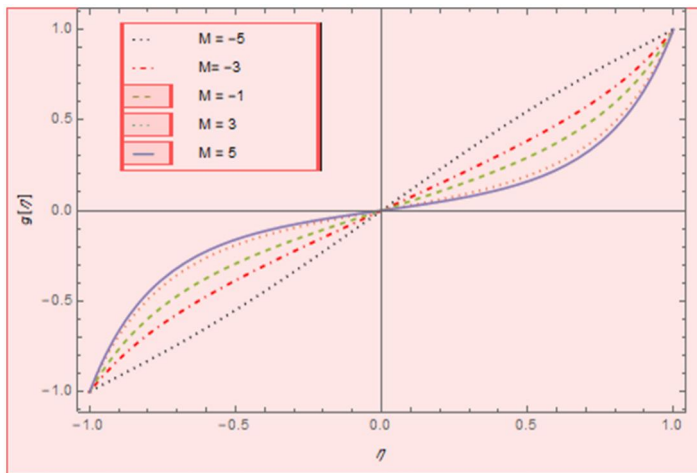


**Figure 3.** Magnetic field impact of tangential velocity profile for  $\alpha = -1, \varphi_1 = \varphi_2 = \varphi_3 = 0.02, Re = 1$ .

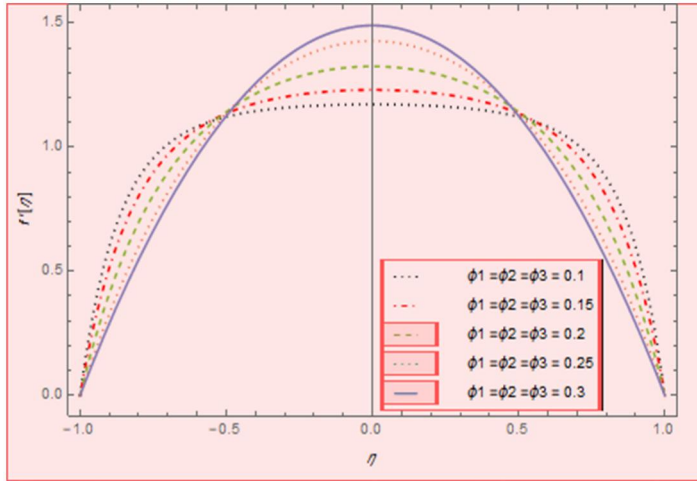


**Figure 4.** Impact of volume fraction parameter over radial velocity profile for  $\alpha = -3$ ,  $M = 2$ ,  $Re = 2$ .

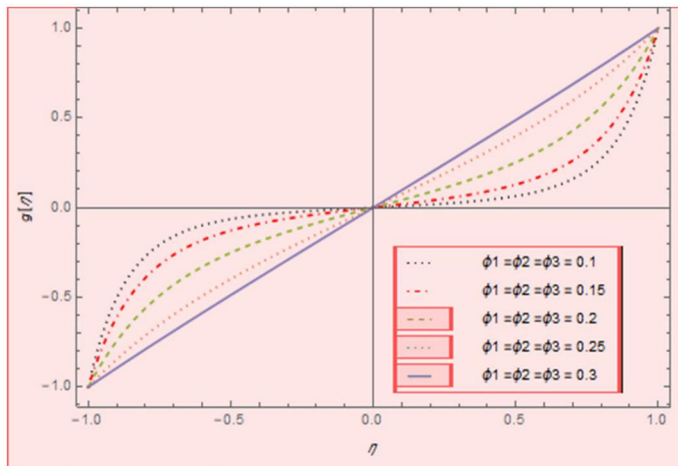


**Figure 5.** Impact of volume fraction parameter over tangential velocity profile for  $\alpha = -3$ ,  $M = 2$ ,  $Re = 2$ .

volume fractions result in a more substantial thickening of the momentum boundary layer. This has practical implications for controlling and optimizing the flow behavior of tri-hybrid nanofluids in various engineering applications. If the number of volume fraction coefficients ( $\phi_1$ ,  $\phi_2$ ,  $\phi_3$ ) is raised while maintaining other parameters ( $\alpha = -3$ ,  $M = 2$ ,  $Re = 2$ ,  $Pr = 6.2$ ) unchanged, it can be observed in [Figure 6](#) that the outflow thermal transmission rate is reduced in the gradient of temperature. The physical behavior indicated by the Prandtl number ( $Pr$ ) in fluid flow is that it influences the relative importance of momentum and thermal diffusivity. When the Prandtl number ( $Pr$ ) increases, it signifies that thermal diffusivity becomes more dominant compared to momentum diffusivity. As a result, the thermal boundary layer's thickness within the top porous disk expands. This reflects how the Prandtl number controls the balance between heat conduction and momentum transfer in the system, ultimately shaping the temperature profile and boundary layer characteristics ([Figure 7](#)).

According to [Figures 8 and 9](#), decreasing the Schmidt number value leads to a drop in the gradient of concentration and border layer thickness for motile microorganisms in the bottom porous disk while raising both in the higher porous disk. The Schmidt number plays a crucial role

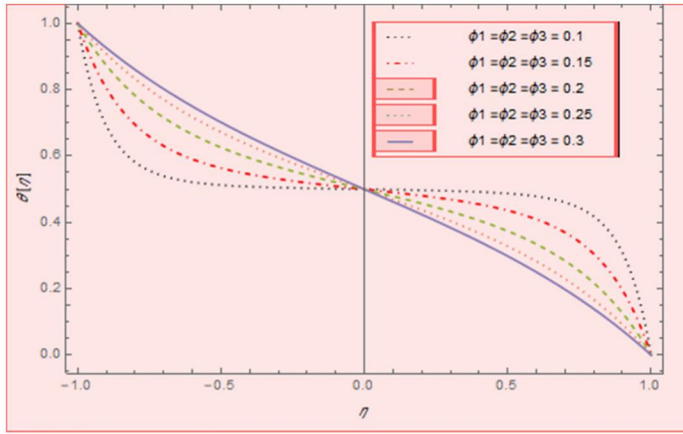


**Figure 6.** Impact of volume fraction parameter over a temperature profile for  $\alpha = -3$ ,  $M = 2$ ,  $Re = 2$ ,  $Pr = 6.2$ .

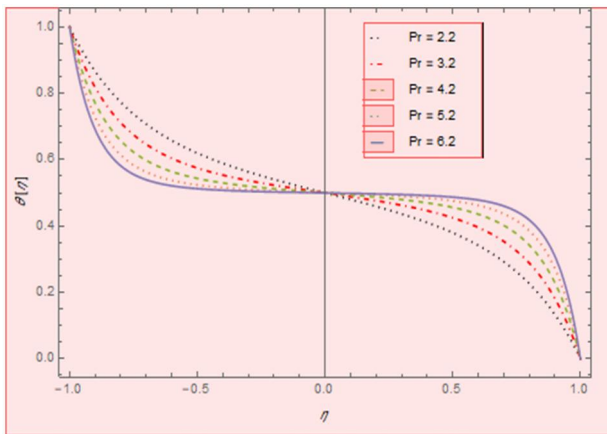


**Figure 7.** Impact of Prandtl number over a temperature profile for  $\alpha = -3$ ,  $M = 2$ ,  $Re = 2$ ,  $\varphi_1 = \varphi_2 = \varphi_3 = 0.02$ .

here as it relates the diffusivity of momentum to the diffusivity of mass in the fluid flow of this system. A lower Schmidt number indicates that the concentration gradient and boundary layer thickness are more influenced by mass diffusion, while a higher Schmidt number emphasizes the impact of momentum diffusion on these characteristics, providing valuable insights into the transport behavior of motile microorganisms within the porous disks. **Figure 10** reveals that elevating the Peclet number ( $Pe$ ) results in a reduction of the border layer thickness for motile microorganisms in both the top and bottom porous disks. In the context of fluid flow within tri-hybrid nanofluids, the Peclet number ( $Pe$ ) serves as a measure of the dominance of convective transport over diffusion. A higher ( $Pe$ ) value signifies an enhanced fluid mixing and a decrease in the boundary layer thickness surrounding the motile microorganisms within the porous disks. The fluid flow is symmetrical.

**Figure 11** provides a physical insight into the behavior of fluid flow in tri-hybrid nanofluids. It illustrates that as the motile microorganism density ( $\gamma$ ) increases, there is a noticeable rise in the thickness of the border layer populated by motile microorganisms near the center of the walls within the top porous disk. This observation highlights the physical significance of motile microorganism density in influencing boundary layer dynamics within the fluid flow, particularly emphasizing how variations in  $\gamma$  impact the spatial distribution of microorganisms and fluid behavior.

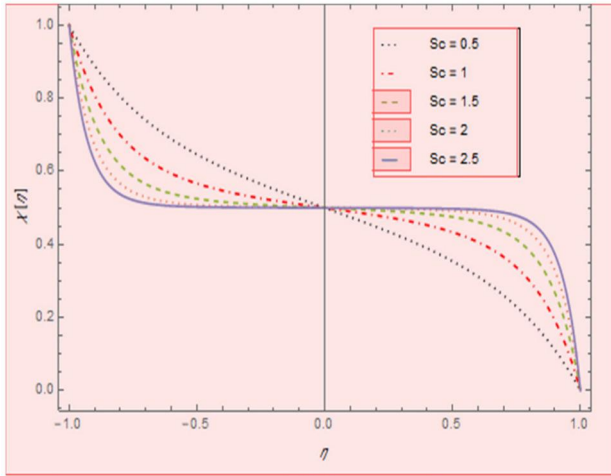


Figure 8. Impact of Schmidt number over concentration profile for  $\alpha = -2$ ,  $Pe = 0.5$ ,  $Re = 2$ ,  $\varphi_1 = \varphi_2 = \varphi_2 = 0.01$ .

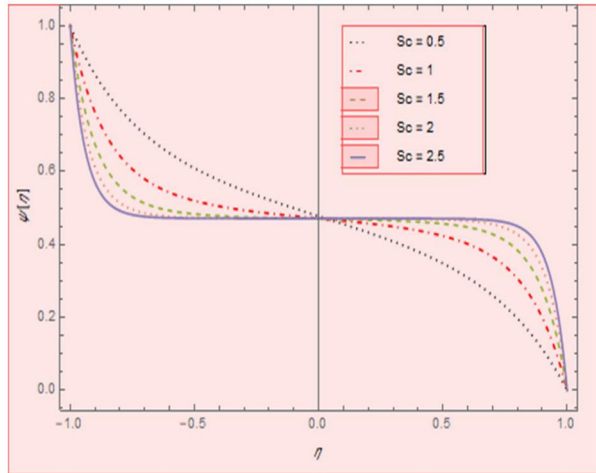


Figure 9. Impact of Schmidt number over motile profile for  $\alpha = -2$ ,  $Pe = 0.5$ ,  $Re = 2$ ,  $\varphi_1 = \varphi_2 = \varphi_2 = 0.01$ ,  $N_2 = 1$ .

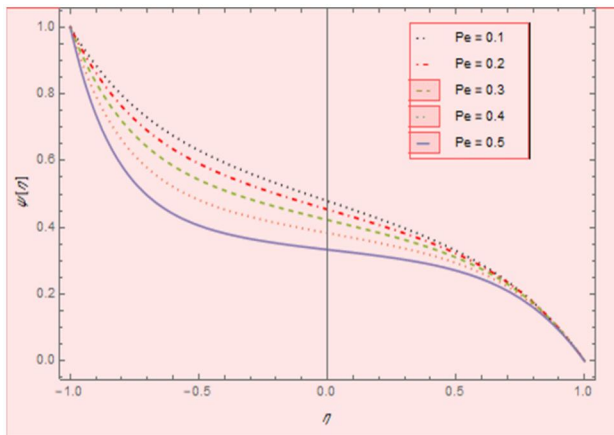
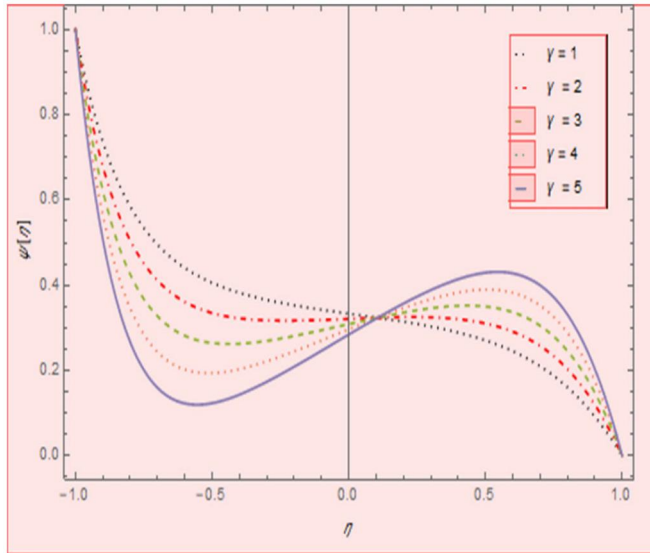


Figure 10. Effect of Peclet number on motile profile for  $\alpha = 2$ ,  $Sc = 1$ ,  $Re = 2$ ,  $\varphi_1 = \varphi_2 = \varphi_2 = 0.01$ ,  $N_2 = 1$ .



**Figure 11.** Effect of density of motile microorganism on motile profile for  $\alpha = 2$ ,  $Sc = 1$ ,  $Re = 2$ ,  $Pe = 0.5$ .

## 5. Conclusions

The time-dependent, three-dimensional, Newtonian fluid, flow of heat, and mass transfer in a tri-hybrid MHD nanofluid of the morphology effect of double porous movable permeable disks. For this, we employ two different types of tri-hybrid nanofluids. Water is the main used base fluid in the study. With it, metallic as well as metallic-oxide NPs were allocated, while checking the influences of multiple nano-dimensional factors over the thickness of the momentum boundary layer, the heat boundary layer, the mass transfer boundary layer, and the motile boundary layer. The numerical and graphical results found in the velocity, temperature, concentration, and motile profiles, are all shown to be significantly influenced by the particle shape. Thus the main conclusions can be as follows:

1. In comparison to various shape factors, including spherical, brick, and cylindrical nanoparticles with form, the maximum thermal conductivity flow of heat transfer is analyzed in tri-hybrid nanofluid ( $Cu + Al_2O_3 + Fe_3O_4/H_2O$ ) platelet of form factor nanoparticles having a volume percentage of 4%.
2. By raising the Schmidt number  $Sc$  along with the density ratio of moving microorganisms' parameter  $\gamma$ , the mass transfer rate, as well as motile microorganisms, is enhanced on the upper porous disk.
3. Volume fraction numbers should be raised to improve the center of the wall thickness for both porous disk and radial velocity profiles.
4. As the permeability Reynolds number  $Re$  as well as the expansion ratio parameter increase numerically, the bottom disk's motile border layer and mass transfer flows progressively grow.
5. If the porous parameter, in addition to the volume fraction of the nanoparticles,  $\phi_1$ ,  $\phi_2$ , and  $\phi_3$  is greater than zero, shear stress, as well as tensional stress transit rates, are enhanced.
6. Increasing the values of the local Reynolds number leads to a reduction in the flow of the skin friction coefficient in the lower disk.
7. By raising the values of the Reynolds number  $Re$  as well as the Schmidt number  $Sc$ , the mass transmission rate on the porous disks is accelerated.
8. When the Peclet number parameter numbers are increased, the flow rates at which mobile microorganisms convey information between the two porous disks are decreased.

## Disclosure Statement

No potential conflict of interest was reported by the author(s).

## Funding

The research is funded by Fundamental Research Funds for the Central Universities (Grant No. D5000230061).

## ORCID

Qadeer Raza  <http://orcid.org/0009-0008-4831-5606>

Ali J. Chamkha  <http://orcid.org/0000-0002-8335-3121>

## References

- [1] M. D. Shamshuddin, N. Akkurt, A. Saeed and P. Kumam, "Radiation mechanism on dissipative ternary hybrid nanofluid flow through rotating disk encountered by Hall currents: HAM solution," *Alex. Eng. J.*, vol. 65, no. 19, pp. 543–559, 2022. DOI: [10.1016/j.aej.2022.10.021](https://doi.org/10.1016/j.aej.2022.10.021).
- [2] K. A. Alharbi, *et al.*, "Computational valuation of darcy ternary-hybrid nanofluid flow across an extending cylinder with induction effects," *Micromachines (Basel)*, vol. 13, no. 4, pp. 588, 2022. DOI: [10.3390/mi13040588](https://doi.org/10.3390/mi13040588).
- [3] S. Alshahrani, *et al.*, "Numerical simulation of ternary nanofluid flow with multiple slip and thermal jump conditions," *Front. Energy Res.*, vol. 10, pp. 967307, 2022. DOI: [10.3389/fenrg.2022.967307](https://doi.org/10.3389/fenrg.2022.967307).
- [4] M. Usman, M. Areshi, N. Khan and M. S. Eldin, "Revolutionizing heat transfer: exploring ternary hybrid nanofluid slip flow on an inclined rotating disk with thermal radiation and viscous dissipation effects," *J. Thermal Anal. Calorim.*, vol. 148, no. 17, pp. 9131–9144, 2023. DOI: [10.1007/s10973-023-12299-7](https://doi.org/10.1007/s10973-023-12299-7).
- [5] F. Ali, A. Zaib, M. I. Khan, F. Alzahrani and S. M. Eldin, "Irreversibility analysis in stagnation point flow of tri-hybrid nanofluid over a rotating disk; application of kinetic energy," *J. Indian Chem. Soc.*, vol. 100, no. 2, pp. 100873, 2023. DOI: [10.1016/j.jics.2022.100873](https://doi.org/10.1016/j.jics.2022.100873).
- [6] G. Gupta and P. Rana, "Comparative study on Rosseland's heat flux on three-dimensional MHD stagnation-point multiple slip flow of ternary hybrid nanofluid over a stretchable rotating disk," *Mathematics*, vol. 10, no. 18, pp. 3342, 2022. DOI: [10.3390/math10183342](https://doi.org/10.3390/math10183342).
- [7] V. Puneeth, *et al.*, "Implementation of modified Buongiorno's model for the investigation of chemically reacting rGO-Fe<sub>3</sub>O<sub>4</sub>-TiO<sub>2</sub>-H<sub>2</sub>O ternary nanofluid jet flow in the presence of bio-active mixers," *Chem. Phys. Lett.*, vol. 786, pp. 139194, 2022. DOI: [10.1016/j.cplett.2021.139194](https://doi.org/10.1016/j.cplett.2021.139194).
- [8] M. K. Sarangi, *et al.*, "Hydrothermal behavior and irreversibility analysis of Bödewadt flow of radiative and dissipative ternary composite nanomaterial due to a stretched rotating disk," *J. Mater. Sci. Eng., B*, vol. 287, pp. 116124, 2023. DOI: [10.1016/j.mseb.2022.116124](https://doi.org/10.1016/j.mseb.2022.116124).
- [9] M. M. Alanazi, *et al.*, "Significance of multi-hybrid morphology nanoparticles on the dynamics of water fluid subject to thermal and viscous joule performance," *Mathematics*, vol. 10, no. 22, pp. 4259, 2022. DOI: [10.3390/math10224259](https://doi.org/10.3390/math10224259).
- [10] A. Tassaddiq, *et al.*, "Heat and mass transfer together with hybrid nanofluid flow over a rotating disk," *AIP Adv.*, vol. 10, no. 5, pp. 055317, 2020. DOI: [10.1063/5.001018.1](https://doi.org/10.1063/5.001018.1).
- [11] X. A. Zhang, *et al.*, "The parametric study of hybrid nanofluid flow with heat transition characteristics over a fluctuating spinning disk," *PLoS One*, vol. 16, no. 8, pp. e0254457, 2021. DOI: [10.1371/journal.pone.0254457](https://doi.org/10.1371/journal.pone.0254457).
- [12] I. Waini, A. Ishak and I. Pop, "Multiple solutions of the unsteady hybrid nanofluid flow over a rotating disk with stability analysis," *Eur. J. Mech. B Fluids*, vol. 94, pp. 121–127, 2022. DOI: [10.1016/j.euromechflu.2022.02.011](https://doi.org/10.1016/j.euromechflu.2022.02.011).
- [13] R. Agrawal and P. Kaswan, "Investigation of the heat performance for squeezed hybrid nanofluid flow between parallel disks embedded in porous medium with thermal radiation," *J. Porous Media*, vol. 25, no. 8, pp. 35–53, 2022. DOI: [10.1615/JPorMedia.2022041525](https://doi.org/10.1615/JPorMedia.2022041525).
- [14] H. Alahmadi and M. O. Alkinidri, "Exploring the impact of nanomaterials on heat and mass transfer properties of Carreau-Yasuda fluid with gyrotactic bioconvection peristaltic phenomena," *Mathematics*, vol. 11, no. 6, pp. 1474, 2023. DOI: [10.3390/math11061474](https://doi.org/10.3390/math11061474).
- [15] J. Iqbal, F. M. Abbasi, M. Alkinidri and H. Alahmadi, "Heat and mass transfer analysis for MHD bioconvection peristaltic motion of powell-eyring nanofluid with variable thermal characteristics," *Case Stud. Thermal Eng.*, vol. 43, pp. 102692, 2023. DOI: [10.1016/j.csite.2022.102692](https://doi.org/10.1016/j.csite.2022.102692).

- [16] T. Akbar, S. Batool, R. Nawaz and Q. M. Zia, "Magnetohydrodynamics flow of nanofluid due to stretching/shrinking surface with slip effect," *Adv. Mech. Eng.*, vol. 9, no. 12, pp. 168781401774026, 2017. DOI: [10.1177/1687814017740266](https://doi.org/10.1177/1687814017740266).
- [17] M. N. Khan, *et al.*, "Irreversibility analysis of ellis hybrid nanofluid with surface catalyzed reaction and multiple slip effects on a horizontal porous stretching cylinder," *Arab. J. Chem.*, vol. 15, no. 12, pp. 104326, 2022. DOI: [10.1016/j.arabj.2022.104326](https://doi.org/10.1016/j.arabj.2022.104326).
- [18] S. Ahmad, *et al.*, "Analysis of heat and mass transfer features of hybrid Casson nanofluid flow with the magnetic dipole past a stretched cylinder," *Appl. Sci.*, vol. 11, no. 23, pp. 11203, 2021. DOI: [10.3390/app112311203](https://doi.org/10.3390/app112311203).
- [19] S. Nadeem, S. Ahmad and M. N. Khan, "Mixed convection flow of hybrid nanoparticle along a riga surface with Thomson and Troian slip condition," *J. Thermal Anal. Calorim.*, vol. 143, no. 3, pp. 2099–2109, 2021. DOI: [10.1007/s10973-020-09747-z](https://doi.org/10.1007/s10973-020-09747-z).
- [20] S. Ahmad, S. Nadeem and M. N. Khan, "Heat enhancement analysis of the hybridized micropolar nanofluid with Cattaneo–Christov and stratification effects," *Proc. Inst. Mech. Eng. C: J. Mech. Eng. Sci.*, vol. 236, no. 2, pp. 943–955, 2022. DOI: [10.1177/09544062211010833](https://doi.org/10.1177/09544062211010833).
- [21] S. G. Bejawada and M. M. Nandeppanavar, "Effect of thermal radiation on magnetohydrodynamics heat transfer micropolar fluid flow over a vertical moving porous plate," *Exp. Comput. Multiph. Flow*, vol. 5, no. 2, pp. 149–158, 2023. DOI: [10.1007/s42757-021-0131-5](https://doi.org/10.1007/s42757-021-0131-5).
- [22] N. S. Khan, *et al.*, "Thermodynamics of second-grade nanofluid over a stretchable rotating porous disk subject to hall current and cubic autocatalysis chemical reactions," *Front. Phys.*, vol. 10, pp. 961774, 2022. DOI: [10.3389/fphy.2022.961774](https://doi.org/10.3389/fphy.2022.961774).
- [23] M. Bilal, *et al.*, "Numerical approximation of microorganisms hybrid nanofluid flow induced by a wavy fluctuating spinning disc," *Coatings*, vol. 11, no. 9, pp. 1032, 2021. DOI: [10.3390/coatings11091032](https://doi.org/10.3390/coatings11091032).
- [24] H. Waqas, R. Naseem, T. Muhammad and U. Farooq, "Bioconvection flow of Casson nanofluid by rotating disk with motile microorganisms," *J. Mater. Res. Technol.*, vol. 13, pp. 2392–2407, 2021. DOI: [10.1016/j.jmrt.2021.05.092](https://doi.org/10.1016/j.jmrt.2021.05.092).
- [25] M. Naveed Khan, S. Ahmad, N. A. Ahammad, T. Alqahtani and S. Algarni, "Numerical investigation of hybrid nanofluid with gyrotactic microorganism and multiple slip conditions through a porous rotating disk," *Waves Random Complex Media*, vol. 30, pp. 1–16, 2022. DOI: [10.1080/17455030.2022.2055205](https://doi.org/10.1080/17455030.2022.2055205).
- [26] U. Khan, *et al.*, "Dynamics of bioConvection Agrawal axisymmetric flow of water-based Cu-TiO<sub>2</sub> hybrid nanoparticles through a porous moving disk with zero mass flux," *Chem. Phys.*, vol. 561, pp. 111599, 2022. DOI: [10.1016/j.chemphys.2022.111599](https://doi.org/10.1016/j.chemphys.2022.111599).
- [27] A. Shahid, H. Huang, M. M. Bhatti, L. Zhang and R. Ellahi, "Numerical investigation on the swimming of gyrotactic microorganisms in nanofluids through porous medium over a stretched surface," *Mathematics*, vol. 8, no. 3, pp. 380, 2020. DOI: [10.3390/math8030380](https://doi.org/10.3390/math8030380).
- [28] T. Hussain, H. Xu, A. Raees and Q. K. Zhao, "Unsteady three-dimensional MHD flow and heat transfer in porous medium suspended with both microorganisms and nanoparticles due to rotating disks," *J. Thermal Anal. Calorim.*, vol. 147, no. 2, pp. 1607–1619, 2022. DOI: [10.1007/s10973-020-10528-x](https://doi.org/10.1007/s10973-020-10528-x).
- [29] A. K. Alzahrani, "Effects of hall current and viscous dissipation on bioconvection transport of nanofluid over a rotating disk with motile microorganisms," *Nanomaterials*, vol. 12, no. 22, pp. 4027, 2022. DOI: [10.3390/nano12224027](https://doi.org/10.3390/nano12224027).
- [30] M. J. Khan, *et al.*, "Numerical analysis of bioconvection-MHD flow of Williamson nanofluid with gyrotactic microbes and thermal radiation: new iterative method," *Open Phys*, vol. 20, no. 1, pp. 470–483, 2022. DOI: [10.1515/phys-2022-0036](https://doi.org/10.1515/phys-2022-0036).
- [31] Y.-M. Chu, M. I. Khan, H. Waqas, U. Farooq, S. U. Khan and M. Nazeer, "Numerical simulation of squeezing flow Jeffrey nanofluid confined by two parallel disks with the help of chemical reaction: effects of activation energy and microorganisms," *Int. J. Chem. React. Eng.*, vol. 19, no. 7, pp. 717–725, 2021. DOI: [10.1515/ijcre-2020-0165](https://doi.org/10.1515/ijcre-2020-0165).
- [32] N. S. Khan, U. W. Humphries, W. Kumam, P. Kumam and T. Muhammad, "Assessment of irreversibility optimization in Casson nanofluid flow with leading edge accretion or ablation," *Z. Angew. Math. Mech.*, vol. 102, no. 10, pp. e202000207, 2022. DOI: [10.1002/zamm.202000207](https://doi.org/10.1002/zamm.202000207).
- [33] O. A. Bég, M. N. Kabir, M. J. Uddin, A. I. M. Ismail and Y. M. Alginahi, "Numerical investigation of von Karman swirling bioconvective nanofluid transport from a rotating disk in a porous medium with Stefan blowing and anisotropic slip effects," *Proc. Inst. Mech. Eng. C: J. Mech. Eng. Sci.*, vol. 235, no. 19, pp. 3933–3951, 2021. DOI: [10.1177/0954406220973061](https://doi.org/10.1177/0954406220973061).
- [34] N. S. Khan, S. Sriyab, A. Kaewkhao and E. Thawinan, "Hall current effect in bioconvection Oldroyd-b nanofluid flow through a porous medium with cattaneo-christov heat and mass flux theory," *Sci. Rep.*, vol. 12, no. 1, pp. 19821, 2022. DOI: [10.1038/s41598-022-23932-0](https://doi.org/10.1038/s41598-022-23932-0).
- [35] M. Shoaib, *et al.*, "Investigation of heat and mass transfer for an MHD hybrid nanofluid flow over a rotating disk: a numerical investigation with supervised neural network," *Waves Random Complex Media*, vol. 30, pp. 1–24, 2022. DOI: [10.1080/17455030.2022.2128228](https://doi.org/10.1080/17455030.2022.2128228).

- [36] S. Chaudhary and K. K. Chouhan, "Convective heat transfer in magnetohydrodynamic  $\text{TiO}_2\text{-CuO}$ /ethylene glycol hybrid nanofluid flow toward stagnation point on a radially stretching disk with thermal radiation," *Heat Transf.*, vol. 51, no. 7, pp. 6320–6339, 2022. DOI: [10.1002/hjt.22593](https://doi.org/10.1002/hjt.22593).
- [37] N. Vijay and K. Sharma, "Magnetohydrodynamic hybrid nanofluid flow over a decelerating rotating disk with Soret and Dufour effects," *MMMS*, vol. 19, no. 2, pp. 253–276, 2023. DOI: [10.1108/MMMS-08-2022-0160](https://doi.org/10.1108/MMMS-08-2022-0160).
- [38] N. S. Khan, P. Kumam and P. Thounthong, "Magnetic field promoted irreversible process of water based nanocomposites with heat and mass transfer flow," *Sci. Rep.*, vol. 11, no. 1, pp. 1692, 2021. DOI: [10.1038/s41598-020-80554-0](https://doi.org/10.1038/s41598-020-80554-0).
- [39] N. T. EL-Dabe, *et al.*, "Non-linear heat and mass transfer in a thermal radiated MHD flow of a power-law nanofluid over a rotating disk," *SN Appl. Sci.*, vol. 1, no. 6, pp. 1–20, 2019. DOI: [10.1007/s42452-019-0557-6](https://doi.org/10.1007/s42452-019-0557-6).
- [40] P. S. Reddy, P. Sreedevi and A. J. Chamkha, "MHD boundary layer flow, heat, and mass transfer analysis over a rotating disk through a porous medium saturated by Cu-water and Ag-water nanofluid with chemical reaction," *Powder Technol.*, vol. 307, pp. 46–55, 2017. DOI: [10.1016/j.powtec.2016.11.017](https://doi.org/10.1016/j.powtec.2016.11.017).
- [41] K. Vajravelu, K. V. Prasad, C. O. Ng and H. Vaidya, "MHD squeeze flow and heat transfer of a nanofluid between parallel disks with variable fluid properties and transpiration," *Int. J. Mech. Mater. Eng.*, vol. 12, no. 1, pp. 1–4, 2017. DOI: [10.1186/s40712-017-0076-4](https://doi.org/10.1186/s40712-017-0076-4).
- [42] N. S. Khan, *et al.*, "Rotating flow assessment of magnetized mixture fluid suspended with hybrid nanoparticles and chemical reactions of species," *Sci. Rep.*, vol. 11, no. 1, pp. 11277, 2021. DOI: [10.1038/s41598-021-90519-6](https://doi.org/10.1038/s41598-021-90519-6).
- [43] S. T. Mohyud-Din, S. I. Khan and B. Bin-Mohsin, "Velocity and temperature slip effects on squeezing flow of nanofluid between parallel disks in the presence of mixed convection," *Neural Comput. Appl.*, vol. 28, no. S1, pp. 169–182, 2017. DOI: [10.1007/s00521-016-2329-1](https://doi.org/10.1007/s00521-016-2329-1).
- [44] C. Ouyang, *et al.*, "Numerical treatment with lobatto IIIA technique for the radiative flow of MHD hybrid nanofluid ( $\text{Al}_2\text{O}_3\text{-Cu}/\text{H}_2\text{O}$ ) over a convectively heated stretchable rotating disk with velocity slip effects," *AIP Adv.*, vol. 10, no. 5, pp. 055122, 2020. DOI: [10.1063/1.5143937](https://doi.org/10.1063/1.5143937).
- [45] R. I. Yahaya, N. M. Arifin, I. Pop, F. M. Ali and S. S. Isa, "Dual solutions for MHD hybrid nanofluid stagnation point flow due to a radially shrinking disk with convective boundary condition," *HFF*, vol. 33, no. 2, pp. 456–476, 2023. DOI: [10.1108/HFF-05-2022-0301](https://doi.org/10.1108/HFF-05-2022-0301).
- [46] N. S. Khan, *et al.*, "Mechanical aspects of maxwell nanofluid in dynamic system with irreversible analysis," *Z. Angew. Math. Mech.*, vol. 101, no. 12, pp. e202000212, 2021. DOI: [10.1002/zamm.202000212](https://doi.org/10.1002/zamm.202000212).
- [47] M. Ramzan, N. S. Khan and P. Kumam, "Mechanical analysis of non-newtonian nanofluid past a thin needle with dipole effect and entropic characteristics," *Sci. Rep.*, vol. 11, no. 1, pp. 19378, 2021. DOI: [10.1038/s41598-021-98128-z](https://doi.org/10.1038/s41598-021-98128-z).
- [48] M. Z. Qureshi, *et al.*, "Dispersion of metallic/ceramic matrix nanocomposite material through porous surfaces in magnetized hybrid nanofluids flow with shape and size effects," *Sci. Rep.*, vol. 11, no. 1, pp. 12271, 2021. DOI: [10.1038/s41598-021-91152-z](https://doi.org/10.1038/s41598-021-91152-z).
- [49] M. Shoaib, *et al.*, "Numerical analysis of 3-D MHD hybrid nanofluid over a rotational disk in presence of thermal radiation with joule heating and viscous dissipation effects using Lobatto IIIA technique," *Alex. Eng. J.*, vol. 60, no. 4, pp. 3605–3619, 2021. DOI: [10.1016/j.aej.2021.02.015](https://doi.org/10.1016/j.aej.2021.02.015).
- [50] A. Ahmadian, M. Bilal, M. A. Khan and M. I. Asjad, "Numerical analysis of thermal conductive hybrid nanofluid flow over the surface of a wavy spinning disk," *Sci. Rep.*, vol. 10, no. 1, pp. 18776, 2020. DOI: [10.1038/s41598-020-75905-w](https://doi.org/10.1038/s41598-020-75905-w).
- [51] M. Alghamdi, "Significance of Arrhenius activation energy and binary chemical reaction in mixed convection flow of nanofluid due to a rotating disk," *Coatings*, vol. 10, no. 1, pp. 86, 2020. DOI: [10.3390/coatings10010086](https://doi.org/10.3390/coatings10010086).
- [52] S. Dinarvand and M. Nademi Rostami, "An innovative mass-based model of aqueous zinc oxide-gold hybrid nanofluid for von kármán's swirling flow," *J. Thermal Anal. Calorim.*, vol. 138, no. 1, pp. 845–855, 2019. DOI: [10.1007/s10973-019-08127-6](https://doi.org/10.1007/s10973-019-08127-6).
- [53] N. S. Khan, U. W. Humphries, W. Kumam, P. Kumam and T. Muhammad, "Dynamic pathways for the bioconvection in thermally activated rotating system," *Biomass Conv. Bioref.*, vol. 9, pp. 1–19, 2022. DOI: [10.1007/s13399-022-02961-9](https://doi.org/10.1007/s13399-022-02961-9).
- [54] Z. Abdelmalek, M. Z. Qureshi, S. Bilal, Q. Raza and E. S. Sherif, "A case study on morphological aspects of distinct magnetized 3D hybrid nanoparticles on fluid flow between two orthogonal rotating disks: an application of thermal energy systems," *Case Stud. Thermal Eng.*, vol. 23, pp. 100744, 2021. DOI: [10.1016/j.csite.2020.100744](https://doi.org/10.1016/j.csite.2020.100744).
- [55] M. Z. Qureshi, *et al.*, "Fractal flow model for cluster interfacial nanolayer of magnetized metallic oxides nanomaterials," *Int. Commun. Heat Mass Transf.*, vol. 139, pp. 106419, 2022. DOI: [10.1016/j.icheatmasstransfer.2022.106419](https://doi.org/10.1016/j.icheatmasstransfer.2022.106419).

- [56] K. Ali, M. Z. Akbar, M. F. Iqbal and M. Ashraf, “Numerical simulation of heat and mass transfer in unsteady nanofluid between two orthogonally moving porous coaxial disks,” *AIP Adv.*, vol. 4, no. 10, pp. 107113, 2014. DOI: [10.1063/1.4897947](https://doi.org/10.1063/1.4897947).
- [57] F. Wang, *et al.*, “A Galerkin strategy for tri-hybridized mixture in ethylene glycol comprising variable diffusion and thermal conductivity using non-Fourier’s theory,” *Nanotechnology*, vol. 11, no. 1, pp. 834–845, 2022. DOI: [10.1515/ntrev-2022-0050](https://doi.org/10.1515/ntrev-2022-0050).
- [58] G. K. Ramesh, “Three different hybrid nanomaterial performances on rotating disk: a non-darcy model,” *Appl Nanosci*, vol. 9, no. 2, pp. 179–187, 2019. DOI: [10.1007/s13204-018-0916-4](https://doi.org/10.1007/s13204-018-0916-4).
- [59] J. Majdalani, C. Zhou and C. A. Dawson, “The two-dimensional viscous flow between slowly expanding or contracting walls with weak permeability,” *J. Biomech.*, vol. 35, no. 10, pp. 1399–1403, 2002. DOI: [10.1016/S0021-9290\(02\)00186-0](https://doi.org/10.1016/S0021-9290(02)00186-0).